

WL-TR-93-2002

PLIF IMAGING OF SPECIES AND  
TEMPERATURE DISTRIBUTIONS IN SPRAY FLAMES

**AD-A260 494**



H.G. ALLEN  
K. DONOHUE  
S.J. DAVIS  
PHYSICAL SCIENCES INC.  
20 NEW ENGLAND BUSINESS CENTER  
ANDOVER, MA 01810

FEB 1990

FINAL REPORT FOR 07/07/89-01/07/90

APPROVED FOR PUBLIC RELEASE; DISTRIBUTION IS UNLIMITED.

**DTIC**  
ELECTE  
FEB 19 1993  
**S E D**

**93-03211**



*56pgs*

**BEST  
AVAILABLE COPY**

AERO PROPULSION AND POWER DIRECTORATE  
WRIGHT LABORATORY  
AIR FORCE SYSTEMS COMMAND  
WRIGHT PATTERSON AFB OH 45433-7650

**93 2 18 337**

## NOTICE

When Government drawings, specifications, or other data are used for any purpose other than in connection with a definitely Government-related procurement, the United States Government incurs no responsibility or any obligation whatsoever. The fact that the government may have formulated or in any way supplied the said drawings, specifications, or other data, is not to be regarded by implication, or otherwise in any manner construed, as licensing the holder, or any other person or corporation; or as conveying any rights or permission to manufacture, use, or sell any patented invention that may in any way be related thereto.

This report is releasable to the National Technical Information Service (NTIS). At NTIS, it will be available to the general public, including foreign nations.

This technical report has been reviewed and is approved for publication.

Sigmund W. Kizirnis

SIGMUND W. KIZIRNIS  
Power Components Branch  
Aerospace Power Division  
Aero Propulsion Directorate

Lowell D. Massie

LOWELL D. MASSIE  
Chief, Power Component Branch  
Aerospace Power Division  
Aero Propulsion and Power Directorate

FOR THE COMMANDER

Michael D. Braydich

MICHAEL D. BRAYDICH, Lt Col, USAF  
Deputy Director  
Aerospace Power Division  
Aero Propulsion & Power Directorate

IF YOUR ADDRESS HAS CHANGED, IF YOU WISH TO BE REMOVED FROM OUR MAILING LIST, OR IF THE ADDRESSEE IS NO LONGER EMPLOYED BY YOUR ORGANIZATION PLEASE NOTIFY WL/POOC-3, WRIGHT-PATTERSON AFB, OH 45433-7650 TO HELP MAINTAIN A CURRENT MAILING LIST.

COPIES OF THIS REPORT SHOULD NOT BE RETURNED UNLESS RETURN IS REQUIRED BY SECURITY CONSIDERATIONS, CONTRACTUAL OBLIGATIONS, OR NOTICE ON A SPECIFIC DOCUMENT.

# REPORT DOCUMENTATION PAGE

Form Approved  
OMB No. 0704-0188

1. AUTHOR(S) 2. REPORT DATE 3. REPORT TYPE AND DATES COVERED 4. FUNDING NUMBERS

5. FUNDING NUMBERS  
C F33615-89-C-2946  
PE 65502  
PR 3005  
TA 21  
WU 38

PLIF IMAGING OF SPECIES AND  
TEMPERATURE DISTRIBUTIONS IN SPRAY FLAMES

M.G. ALLEN  
K. DONOHUE  
S.J. DAVIS

PHYSICAL SCIENCES INC.  
20 NEW ENGLAND BUSINESS CENTER  
ANDOVER, MA 01810

AERO PROPULSION AND POWER DIRECTORATE  
WRIGHT LABORATORY  
AIR FORCE SYSTEMS COMMAND  
WL/POOC, Attn: KIZIRNIS 513-2555179  
WRIGHT-PATTERSON AFB OH 45433-7650

10. DISTRIBUTION STATEMENT  
WL-TR-93-2002

APPROVED FOR PUBLIC RELEASE; DISTRIBUTION IS  
UNLIMITED.

12. DISTRIBUTION CODE

This Phase I SBIR program investigated the application of Planar Laser-Induced Fluorescence (PLIF) to measurements of species concentration and temperature distributions in liquid-fueled spray flames. A bench-top spray burner was constructed and characterized with n-heptane fuel. Using laser sheet illumination, time-averaged and instantaneous distributions of the OH radical were obtained. Ratios of time-averaged OH distributions obtained from two isolated rotational levels were used to infer the time-averaged temperature in the hot, combustion product gases. Comparison of the PLIF temperature data with thermocouple scans suggest the technique is accurate to within about 5 percent. Time-averaged and mean distributions of NO seeded into the primary, atomizing air stream were also obtained. Preliminary ratios of two NO PLIF images obtained from separate rotational excitation were used to infer

PLIF, LASER-INDUCED FLUORESCENCE, OH, NO,  
PHOTODISSOCIATION, C H , LIF THERMOMETRY

13. NUMBER OF PAGES

14. PRICE CODE

UNCLASSIFIED

UNCLASSIFIED

UNCLASSIFIED

UL

temperature in the cold, evaporating region of the flame. Initial relative temperature distributions appear correct, but further work is required to recover the absolute level. Using multiphoton photodissociation, instantaneous measurements of the  $C_2H_2$  (and potentially other hydrocarbon fragments) were obtained in the pyrolyzing region of flame. The technique also revealed the instantaneous structure of the reaction zone.

Accession For	
NTIS CRA&I	<input checked="" type="checkbox"/>
DTIC TAB	<input type="checkbox"/>
Unannounced	<input type="checkbox"/>
Justification	
By	
Distribution /	
Availability Codes	
Dist	Avail and/or Special
A-1	

DTIC QUALITY ASSURANCE

## TABLE OF CONTENTS

<u>Section</u>	<u>Page</u>
1. INTRODUCTION	1
2. BACKGROUND	3
2.1 Laser-Induced Fluorescence	3
2.2 Temperature Measurements Based on Laser-Induced Fluorescence	7
2.3 LIF Strategies for OH and NO in Spray Flames	10
2.3.1 OH Fluorescence	10
2.3.2 NO Fluorescence	17
2.4 Multiphoton Photodissociation of C <sub>2</sub> H <sub>2</sub>	21
3. EXPERIMENTAL SETUP	25
3.1 Spray Flame Apparatus	26
3.2 Laser Systems	30
3.3 Imaging Detector System	31
4. RESULTS AND DISCUSSION	32
4.1 OH and OH-Based Temperature Measurements	32
4.2 NO and NO-Based Temperature Measurements	39
4.3 C <sub>2</sub> H <sub>2</sub> Photodissociation Measurements	44
5. CONCLUSIONS AND RECOMMENDATIONS	47
6. REFERENCES	49

## LIST OF FIGURES

<u>Figure No.</u>		<u>Page</u>
1	Schematic Energy Level Diagram Showing Important Processes in Laser-Induced OH Fluorescence	4
2	Common Upper Level Scheme for OH LIF Temperature Determination	9
3	Typical Responsivity of an S-20 Extended UV Photocathode	11
4	OH Fluorescence Collection	12
5	Schematic Energy Level Diagram Showing Important Processes in Laser-Induced NO Fluorescence	19
6	NO Fluorescence Transmission	19
7	Energy Level Diagram Showing Relevant Processes for Multiphoton Photodissociation of Acetylene	22
8	Diagram of Five-Level Photodissociation Model	23
9	Schematic Diagram of Typical PLIF Experimental Setup	25
10	Schematic Diagram of Spray Flame Apparatus	27
11	Photograph of Instantaneous Droplet Spatial Distribution in Gold Spray	28
12	A Partial Excitation Spectrum of the (1,0) Band of the OH A-X System	32
13	A Boltzmann Plot of the Peak Fluorescence from Several Isolated Liens in the Spectrum of Figure 12	33
14	OH PLIF Image in Central Plane of Spray Flame	34
15	Temperature Image Inferred from the Ratio of $Q_1(5)$ Excitation and $Q_1(12)$ Excitation in OH	36
16	Comparison Between PLIF and Thermocouple Temperature Determinations	38
17	Instantaneous and Average Distributions of NO Seeded Into the Primary Air Stream of the Spray Flame	40
18	Comparison of NO PLIF Images in Non-Burning Jets With and Without Droplets	41

# LIST OF FIGURES (Continued)

<u>Figure No.</u>		<u>Page</u>
19	Temperature Determination from NO PLIF	42
20	Acetylene Photodissociation Image	44
21	PMPD Image of the Detailed Reaction Zone Structure Near the Vicinity of the Primary Flame Zone	46

## 1. INTRODUCTION

Combustors lie at the heart of virtually all flight vehicles and combustor performance continues to be a major contributor to an aircraft's ultimate operating characteristics. The vast majority of these combustors burn liquid fuels, typically a hydrocarbon derivative. As such, the understanding of the complex interactions between an evaporating liquid spray and a reacting gaseous flowfield is critical in optimization of combustor performance. In addition to the analytical difficulties of such a system, experimental study is also hampered by the complexity of the multi-phase, high-temperature flow.

The scalar fields of droplet distribution, species concentrations, and temperature are important experimental parameters which must be measured in order to understand the dynamics of the reacting system or, indeed, to simply characterize a given configuration. Traditional, intrusive measurement techniques for temperature and species concentration rely on the insertion of physical probes (thermocouple or gas-sampling) into the flowfield. In addition to the conventional limitations of these approaches in gaseous flows, is added the difficulty of interpreting the results in the presence of liquid droplets. Thermocouples, for example, do not yield reliable results in regions of impinging droplets.

Non-intrusive, optical diagnostic techniques for reacting flows have undergone extensive development during the past decade. In particular, techniques based on laser sheet illumination have demonstrated the ability to obtain instantaneous, two-dimensional distributions of flow properties. These techniques have recently been reviewed by Hanson.<sup>1,2</sup> Notably absent from much of this work, however, are techniques specifically tailored for the demands of spray flames (cf., reference 3).

This report details the approach and results from a Phase I SBIR program to develop techniques for two-dimensional imaging of property distributions in spray flames. The Phase I effort focused on demonstration of several species concentration imaging techniques and temperature imaging. The program augments



earlier published work by extension to new parameters and incorporates state-of-the-art imaging detector arrays.

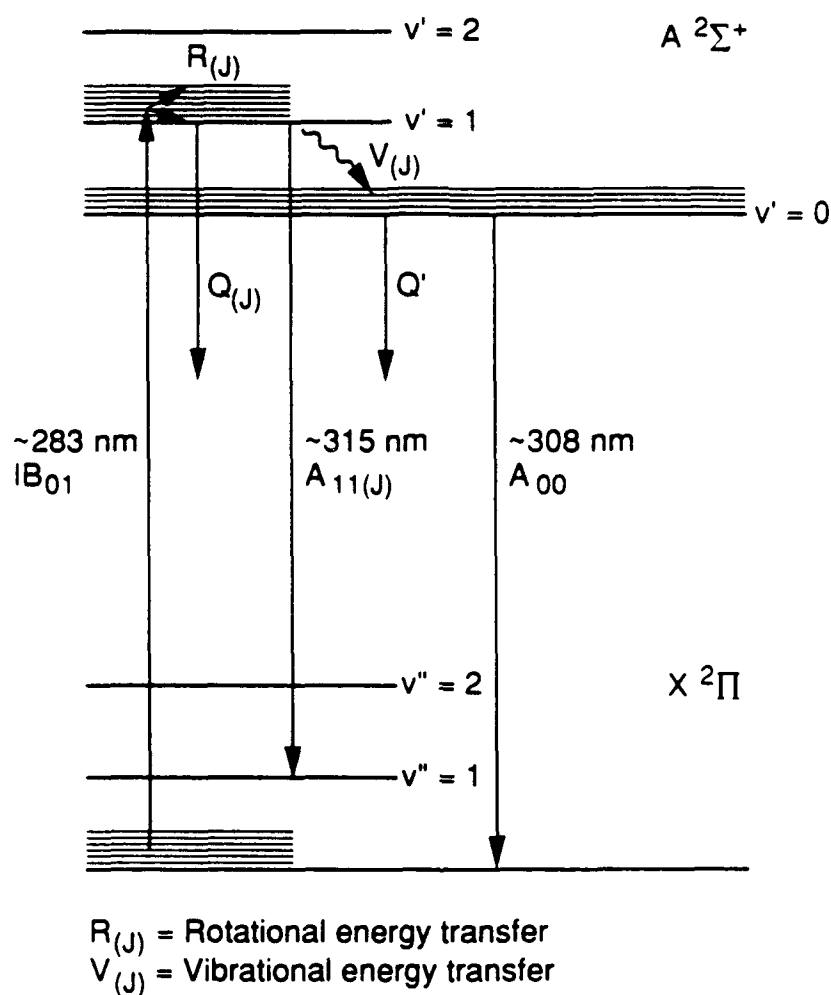
## 2. BACKGROUND

The diagnostics developed in this program are based on Planar Laser-Induced Fluorescence (PLIF). This section describes the theoretical approach to LIF and how it is tailored for applications to spray flames. Temperature determination based on LIF is also described. Specific strategies for LIF monitoring of OH and NO are presented in detail, along with the relevant parameters used to reduce the fluorescence signal to concentration and temperature. Finally a variation of PLIF, Planar Multiphoton PhotoDissociation (PMPD), is described with application to measurements of  $C_2H_2$ .

### 2.1 Laser-Induced Fluorescence

The basic physics of LIF can be understood with reference to Figure 1. This diagram shows the relevant energy levels and dynamic processes in LIF of OH. Laser light, typically derived from a pulsed, tunable dye laser, is tuned into resonance with an isolated rovibronic transition of the molecule of interest. For reasons discussed in greater detail in Subsection 2.3, we show this transition in Figure 1 as originating from the ground vibrational level ( $v'' = 0$ ) in the lower electronic state ( $X^2\Pi$ ) and terminating in the first excited vibrational level ( $v' = 1$ ) of the upper electronic state ( $A^2\Sigma^+$ ). The laser light couples the two levels via absorption and stimulated emission.

A net transfer of population from the ground state to the upper state occurs. Additional decay paths, not involving the laser field, exist for the molecules in the upper state. At atmospheric pressure, the dominant path is collisionally induced electronic quenching, a non-radiative decay path. Non-radiative energy transfer redistributes population from the directly excited level to various upper rotational and, in the example shown, to other vibrational levels. Spontaneous radiative decay also occurs. This spontaneous emission of photons is radiated away from the excitation volume. It is collected by appropriate detection systems and constitutes the fluorescence signal.



B-1807

Figure 1. Schematic Energy Level Diagram Showing Important Processes in Laser-Induced OH Fluorescence

The relationship between the detected fluorescence signal and the parent species number density depends, in general, on the type of laser employed, the laser intensities involved, and spectroscopic parameters particular the molecule or atom under study. For the conditions relevant to this study, we can use the so-called broadband, low-intensity approximation<sup>4</sup> and write

$$S_F = (I_v B) \cdot (F_y) \cdot (f_B N_t V_c) \cdot \left( \eta \frac{\Omega}{4\pi} \right) \quad (1)$$

where

$I_v$  = laser spectral fluence

$B$  = Einstein B coefficient for absorption

$F_y$  = fluorescence yield

$f_B$  = Boltzmann population fraction

$N_t$  = species number density

$V_c$  = collection volume

$\eta$  = filter transmission, detector responsivity, etc.

$\Omega$  = collection solid angle of imaging system.

The primary assumptions in this model are

1. The laser spectral bandwidth is larger than the molecular absorption lineshape. For the pulsed dye lasers used in this study, typical spectral bandwidths are on the order of 15 GHz. By comparison, absorption linewidths for OH and NO in atmospheric pressure flames are less than 10 GHz. The absorption linewidth will increase somewhat with pressure so that at pressures above several atmospheres, explicit treatment of the overlap with the laser spectral bandwidth may be required.
2. The rate of stimulated emission and absorption,  $I_v(B_{21} + B_{12})$ , is much less than rate of non-radiative (or any other) decay rate. For atmospheric pressure flames, the total rate of collisional energy transfer, including rotational and vibrational transfer, and collisional quenching, is on the order of  $10^9$  to  $10^{10} \text{ s}^{-1}$ . As will be discussed in later sections, typical stimulated transition rates are on the order of  $10^9 \text{ s}^{-1}$ . Hence, we may not be entirely within the linear fluorescence regime. This does not, in principle, effect the quantitateness of the fluorescence signal, since the signal is still linearly related to the species number density, but may complicate the use of fluorescence data for temperature determinations since different transitions may saturate at different power levels.

The primary difficulty in obtaining PLIF images in spray flames arises from interference by the liquid fuel droplets. This interference manifests itself in two forms: removal (absorption) or redistribution (scattering) of the energy in the laser sheet resulting in non-uniform excitation in the field of view, and elastic scattering from the droplets into the fluorescence collection system. With regard to energy removal from the laser sheet, most distillate fuels are transparent in the visible and near-UV spectrum (this is true of the fuel used in this study - heptane) and we may neglect absorption. For droplet diameters,  $d_p$ , substantially larger than the wavelength of the incident radiation (i.e.,  $d_p > 10 \mu\text{m}$ ), we may approximate the gross scattering behavior using geometric optics. Essentially all of the scattered light is contained in the first few lobes of the Fraunhofer diffraction pattern. A useful formula for estimating the half-angle of the first three lobes is

$$\Theta = \frac{10 \lambda}{\pi d_p} \quad . \quad (2)$$

Thus, for a  $50 \mu\text{m}$  droplet and  $\lambda = 250 \text{ nm}$ ,  $\Theta \approx 1 \text{ deg}$ . This small angular deviation does not significantly effect the energy distribution within the sheet over the regions imaged in this study.

The second and more severe interference is from the elastically scattered light which is collected by the imaging optics, which is generally several orders of magnitude greater than the fluorescence. The elastic scattering, however, occurs only at the laser wavelength, while the fluorescence occurs at the wavelengths of all the allowed transitions from the excited states. Thus, the scattering interference can often be eliminated by spectral filtering, if an appropriate excitation/detection strategy is chosen that separates the laser wavelength from the fluorescence wavelengths. The individual strategies that we developed for measurements of OH and NO are discussed in detail in Subsection 2.3.

## 2.2 Temperature Measurements Based on Laser-Induced Fluorescence

Equation (1) shows that the fluorescence signal is related to the number density of an isolated rovibrational level,  $f_B N_t$ . For a system in thermodynamic equilibrium, the Boltzmann population fraction may be written as

$$N_{J''}/N_T = \frac{2J'' + 1}{Q} \cdot e^{-E_t/kT} \quad (3)$$

where

$N_{J''}$  = number density in rotational level  $J''$

$Q$  = molecular partition function

$E_t$  = total term energy of state pumped.

For the purposes of a single PLIF image, where it is desired to have the data be proportional to mixture fraction and not temperature, it is possible to select an initial  $J$ -level that minimizes the temperature dependence over the range of expected temperatures. This is found by differentiating Eq. (3) with respect to  $T$ , setting the result equal to zero, and solving for the resultant  $J$ . For rigidly rotating molecules, this formula is

$$J^* = 0.59 \sqrt{\frac{T(K)}{B(\text{cm}^{-1})}} \quad (4)$$

For OH,  $B \approx 18 \text{ cm}^{-1}$ , and  $J^* \approx 6.5$  near 2000 K. For NO,  $B \approx 1.7 \text{ cm}^{-1}$ , and  $J^* \approx 14.5$  near 1000 K. Typically, the population of nearby  $J$ -levels have only weak temperature dependence.

The LIF-based temperature measurement technique is anchored to the temperature dependence of the Boltzmann distribution. Sequential measurements of the population in isolated rotational levels can be plotted against the rotational energy,  $BJ''(J'' + 1)$ , in the following manner

$$\ln \left[ \frac{N_{J''}}{2J'' + 1} \right] = A - \frac{1}{kT} \cdot B J''(J'' + 1) \quad (5)$$

to yield a straight line of slope  $1/kT$ . Alternatively, any pair of population measurements may be used to form a two-point estimate of the slope of this line.

The populations are actually determined by fluorescence measurements. Using Eq. (1) to replace the number density in a particular level with the fluorescence signal from that level, we have

$$\ln \left\{ \frac{S_{Fu}}{S_{FL}} \cdot \frac{F_{yL}}{F_{yu}} \cdot \frac{B_L}{B_u} \cdot \frac{(2J'' + 1)_L}{(2J'' + 1)_u} \right\} = \frac{-\Delta E}{kT} \quad (6)$$

The subscripts u and L refer to the upper and lower rotational levels within the ground vibrational level being probed by the laser.

This program investigated the use of both OH and NO fluorescence for temperature determination. Each species has a different range of flame conditions over which we can expect to observe fluorescence signals and, hence, provides the opportunity to measure temperature in different regions of the flame. The OH radical is a high-temperature combustion product and can be used to measure temperature in the post-reaction zones of the flame. The NO radical was introduced into the atomizing air stream and was eventually consumed in the reaction zone. Thus, the NO fluorescence could be used to determine temperature in the low-temperature evaporating and pyrolyzing regions of the flame.

A first-order error analysis of Eq. (6) yields the following expression for the uncertainty in the inferred temperature as a function of the uncertainty in the fluorescence signal itself:

$$\frac{\sigma T}{T} = \frac{kT}{\Delta E} \cdot \frac{\sigma(S_{Fu}/S_{FL})}{S_{Fu}/S_{FL}} \quad (7)$$

Equation (7) shows that the limiting uncertainty decreases as the energy separation between the two rotational levels increases. An ideal situation would be if the two lower rotational levels were excited to the same upper rotational level so that the fluorescence yield,  $F_y$ , was constant. For both OH and NO, rotational selection rules require that such a scheme use a P-R doublet, as shown in Figure 2.

While in principle this is a valid approach, the separation between the two ground state rotational states is limited (in first order) to

$$\Delta v [R(J-1) - P(J+1)] = 4B(J + 1/2) \quad .$$

For OH at a temperature of 2000 K,  $kT \sim 1300 \text{ cm}^{-1}$ . Equation (7) shows that the temperature uncertainty is just the fluorescence uncertainty multiplied by the factor  $kT/\Delta E$ . For no amplification of the fluorescence uncertainty

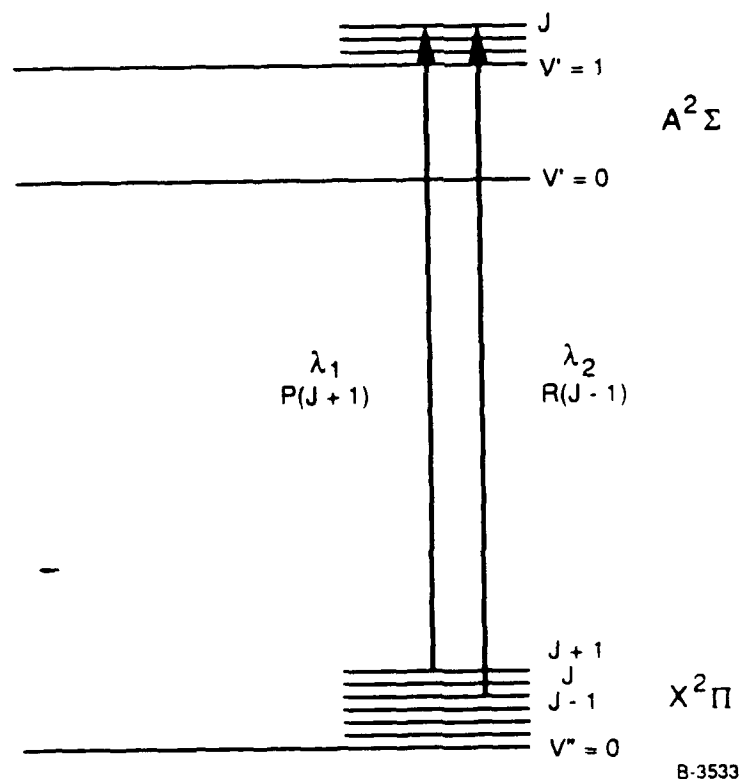


Figure 2. Common Upper Level Scheme for OH LIF Temperature Determination



( $\Delta E/kT \sim 1$ ), the constraint of common upper states requires  $J \sim 19$ . Even at 2000 K, this level is relatively unpopulated, consequently signal levels would be very small and the uncertainty in the fluorescence ratio concomitantly high. In practice, the availability of such line pairs for both OH and NO is severely restricted by lack of resolution between overlapping transitions.

### 2.3 LIF Strategies for OH and NO in Spray Flames

#### 2.3.1 OH Fluorescence

The A-X system of OH possesses many strong transitions in the wavelength region near 300 nm, easily accessed by frequency-doubled, tunable dye-lasers. Excitation or detection of fluorescence from an off-diagonal transition of this system (i.e., where  $\Delta v$  is not equal to zero) allow wide wavelength separation between the elastically scattered laser radiation and the collected fluorescence signal. In evaluating potential strategies, it is useful to define a figure of merit from Eq. (1). Such a figure is defined as

$$\text{Figure of Merit} = \eta EBA$$

where  $\eta$  is the quantum efficiency of the intensifier photocathode at the fluorescence wavelength,  $E$  is the laser pulse energy, and the remaining constants are as in Subsection 2.2.

This figure of merit, then, is proportional to the photocathode current in the intensifier and is a direct measure of the signal strength. Strategies which maximize this figure will result in the highest signal levels on the photodetector. We will take as a typical response curve, the specifications of an ITT S-20 extended UV photocathode, shown in Figure 3.

At flame temperatures, the population of the first excited vibrational state is only a few percent of the ground vibration state, so any reasonable strategy will excite a transition originating in the ground vibrational state. Off-diagonal transitions in this system are relatively strong, but decrease

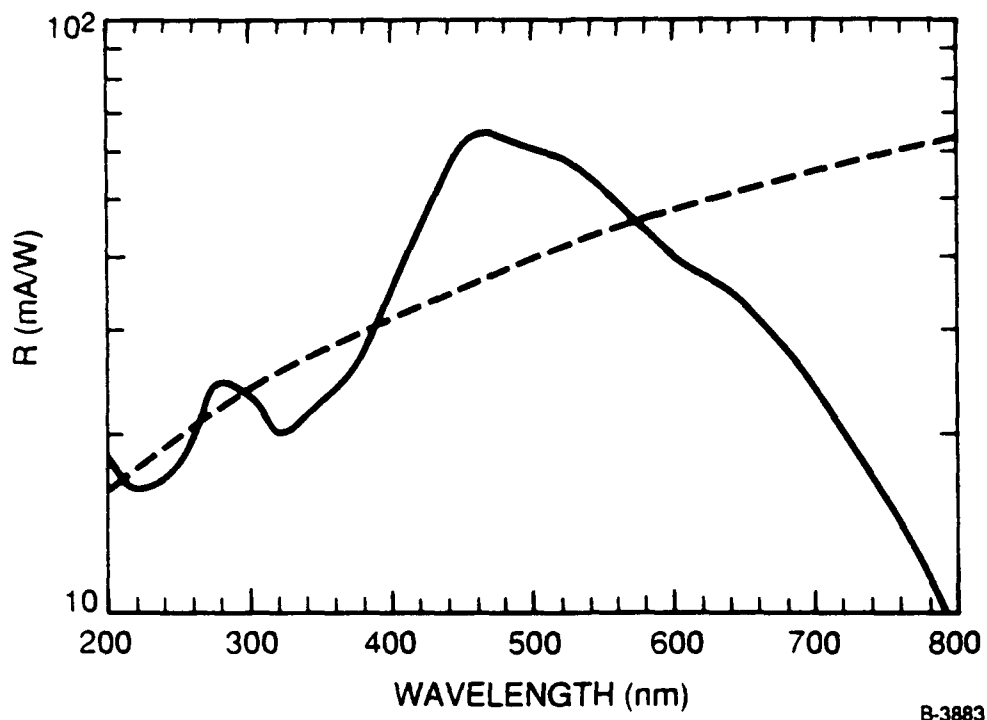


Figure 3. Typical Responsivity of an S-20 Extended UV Photocathode (solid line). A 10% quantum efficiency curve (dashed line) is shown for reference.

rapidly with increasing  $\Delta v$ . Detailed examination of the OH system indicates two possible choices for non-resonant excitation/detection:

1. Exciting in the (0,0) band (near 308 nm) and detecting the (0,1) band (near 346 nm) or
2. Exciting in the (1,0) band (near 280 nm) and detecting the (1,1) band (near 315 nm).

The choice of rotational level and transition is usually governed by the rotational population fraction at a given temperature and the line strength for the allowed branches from that level. For temperatures around 1800 K, the rotational population distribution reaches a broad maximum between  $J = 4.5$  and  $J = 7.5$ . The Q-branch tends to be the strongest branch at these values of  $J$ ,

so we consider the  $Q_1(5)$  transition for comparison purposes. Einstein A and B coefficients for isolated OH transitions are tabulated by Chidsey and Crosley.<sup>5</sup> Using values contained in this reference and assuming typical pulse energies available from Nd:YAG-pumped dye lasers, we find the figure of merit for strategy 1 to be  $1.3 \times 10^{-16}$  and for strategy 2 to be  $7.4 \times 10^{-15}$ . Hence strategy 2 is more than 50 times more sensitive than strategy 1 and was selected for this application.

Figure 4 shows the filter transmission function used for the OH PLIF along with sketches of the (1,1) and (0,0) band fluorescence. Reference to Figure 1 shows that, although we excite  $v' = 1$ , downward vibrational energy transfer results in significant population of the  $v' = 0$  level with subsequent fluorescence in the (0,0) band. Both radiative channels are detected using the filter function shown. This filter was a combination of two Schott Glasses (UG-5 and WG-320). The transmission function was measured at PSI using a scanning spectrophotometer.

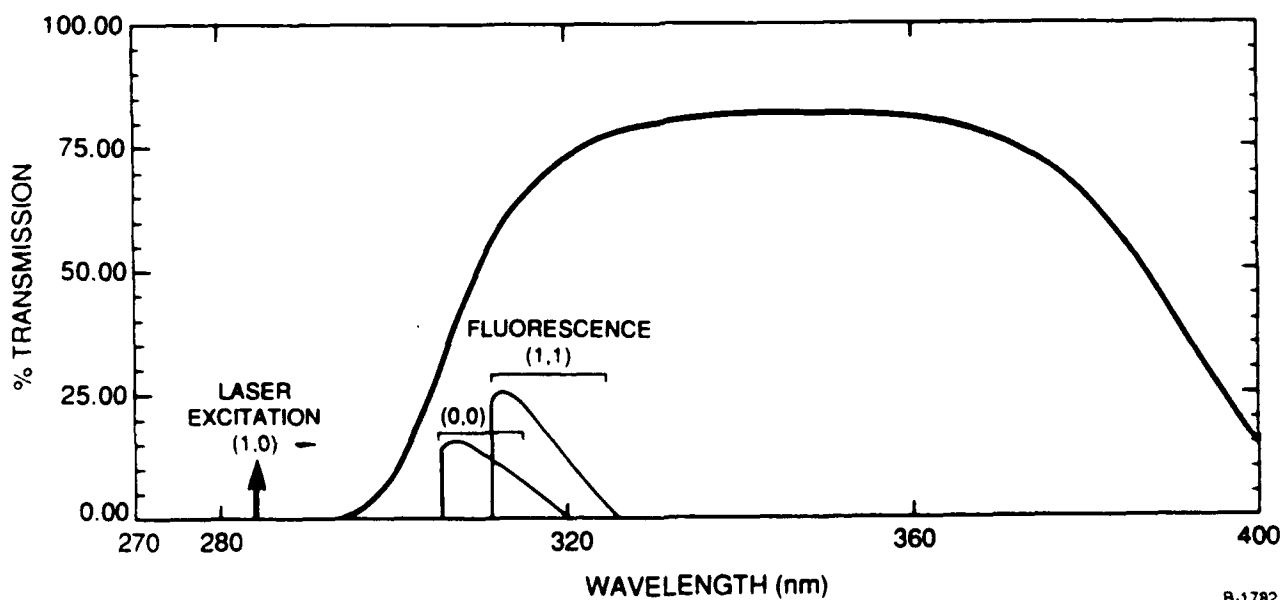


Figure 4. OH Fluorescence Collection

The energy level diagram of Figure 1 shows the relevant kinetic processes which must be understood in order to calculate the fluorescence yield. They are defined as follows:

- $Q(J)$   $\equiv$  quenching rate of laser-excited  $v'=1$  level
- $R(J)$   $\equiv$  rate of rotational energy transfer within  $v'=1$
- $V(J)$   $\equiv$  rate of vibrational energy transfer from  $v'=1$  to  $v'=0$
- $Q'$   $\equiv$  rate of electronic quenching from  $v'=0$
- $A_{11}(J)$   $\equiv$  radiative rate for (1,1) band
- $A_{00}$   $\equiv$  radiative rate for (0,0) band.

The (J) indicates that rate is a function of the initial J-level excited by the laser. Fortunately, the kinetics of the  $A^2\Sigma^+$  state in OH in atmospheric pressure flames are reasonably well understood. Crosley and coworkers<sup>6-10</sup> have completed numerous, detailed studies and have determined many relevant kinetic rates. Thus  $R(J)$ ,  $V(J)$ ,  $Q(J)$  and  $A_{v',v''}$  are known for a variety of conditions. We use these results to guide the prediction of the fluorescence yield that is particularly important for the extraction of temperature using the two-line LIF method.

Rotational energy transfer (RET) within the laser excited  $v'=1$  level is perhaps the most important source of uncertainty since we excite two distinct J levels in the temperature determination. Early attempts at OH thermometry in the literature were severely biased by RET effects. This work generally used narrow-band detection for the fluorescence monitor. Since each J level fluoresces at a distinct wavelength, RET caused a shift in the emission wavelength. For sufficiently narrow-band detection, some of the fluorescence from collisionally populated levels is undetected and errors result in the inferred temperature. In the current approach, we detect essentially all of the fluorescence from both the (1,1) and (0,0) bands, thus mitigating these effects. However, accurate filter transmission curves are required in order to reduce the LIF data.

If quenching were the only non-radiative term, then the fluorescence yield would simply be

$$F_y = \frac{A}{A + Q} \quad (8)$$

However, for our excitation/detection strategy, the fluorescence yield is determined by writing four-level rate equations and assuming a steady-state. This results in a yield of the following form

$$F_y = \frac{f_{(\lambda)} A_{11}(J) + f_{(\lambda)} A_{00} (N_0/N_1)}{Q(J) + V(J)} \quad (9)$$

where

$f_{(\lambda)}$  = the filter transmission at  $\lambda$   
 $N_0/N_1$  = fractional population in  $v'=0$ .

The first term in the numerator is the rate of radiative emission from the  $v'=1$  state multiplied by the appropriate filter transmission at that wavelength. The second term is the rate of radiative emission from the  $v'=0$  state multiplied by the filter transmission at this wavelength and multiplied by the fractional population which resides in this level at steady-state.

In order to use Eq. (9), we have made several assumptions about the role of energy transfer. For simplicity we have assumed a frozen rotational distribution in the excited state. We can evaluate this assumption based on measured and calculated values of  $A/Q$  ratios in  $v'=0$ . It is instructive to compare the measured ratio to those calculated with the imposed limits of complete thermal redistribution and no rotational redistribution. For a thermal distribution at 1900 K and atmospheric pressure, the calculated  $A/Q$  ratio is  $6.9 \times 10^{-3}$ . The measured distributions (Ref. 6) were for excitation

of  $J'=10.5$  and we calculate an  $A/Q$  of  $8.27 \times 10^{-3}$ . In the limit of no rotational distribution, we calculate  $A/Q = 8.55 \times 10^{-3}$ . The frozen distribution is only 3 percent greater than the actual distribution while a thermal distribution gives an  $A/Q$  16 percent less. Hence, the population is peaked around the directly excited level and is close to frozen, justifying our assumption.

Modeling of the rotational transfer processes in the upper state by Crosley suggests that the fractional population in the laser excited  $J'$  level (not the fluorescence from that state) varies linearly from 9 percent at  $J'=0$  to 32 percent at  $J'=15$  in atmospheric pressure flames.<sup>7</sup> The reason for this variation is the decrease in  $R$  with increasing  $J$ . Hence, the  $J'=10$  excitation is closer to the frozen case than the thermal case. For excitation at lower  $J$ , we would expect the distribution to be more thermalized. However, the temperature measurements are usually made using  $J$ 's of 5 to 15, so we choose the frozen distribution.

The rate of vibrational energy transfer (VET) from  $v'=1$  to  $v'=0$  is dependent on the initial  $J'$  level excited in the A state. This rate varies linearly with the  $J'$  level and its dependence on  $J'$  has been reported as the ratio of population in  $v'=0$  to  $v'=1$ .<sup>8</sup> (Upward vibrational energy transfer is assumed to be insignificant.)

The  $J$ -dependent  $A$ -coefficients for the initially excited levels in the upper state are tabulated in Ref. 5. For population transferred to  $v'=0$ , we rely on the observation that the rotational distribution in  $v' = 0$  is thermal and independent of the initial  $J$  level excited in  $v'=1$  (Ref. 9). We have chosen the value of  $A_{00}$  at  $J'=5.5$  as an average value which we use for all excited lines. —

Lastly, we have estimated rates of electronic quenching from  $v'=1$  and  $v'=0$  in the excited state. These quenching rates are dependent on rotational level in the respective vibrational level, the quenching partner, and the gas temperature. Reported values for the quenching rates in the rotational manifolds of both vibrational levels comprise an incomplete data set. (In fact, absolute

rates of J-dependent quenching in  $v'=1$  have not been reported for  $H_2O$ , the dominant quencher in flame environments.) Some data exist, however, for the  $v'=0$  level which allowed us to estimate the rates of quenching in  $v'=0$  and  $v'=1$  for J levels particular to our data.

Given that the rotational distribution in  $v'=0$  following vibrational transfer is nearly independent of the initial J pumped, it is sufficient to select a single value of quenching to characterize this state. We use the typical value of  $5.6 \times 10^8 \text{ s}^{-1}$  to characterize the quenching from  $v'=0$ .<sup>10</sup> For excitation to  $v'=1$ ,  $v'=0$  is populated only by VET, so the contribution to the total fluorescence yield is weighted by the amount of transfer, i.e., by the ratio  $N_0/N_1$ , which is dependent on the initial J' excited in  $v'=1$ . These values have been reported by Smith and Crosley.<sup>8</sup>

Estimating quenching rates from  $v'=1$  is more problematic. We assume a J-dependence which is identical to that in  $v'=0$  and scale the typical value for  $v'=0$  accordingly. To this end, we assume a linear variation in quenching of  $v'=0$  which is decreasing with increasing J. Given room temperature quenching cross sections for  $H_2O$ , a dominant quencher in most flames, ( $93 \text{ Angstroms}^2$  for  $J=0$  and  $82 \text{ Angstroms}^2$  for  $J = 5$ ),<sup>9</sup> we can construct a linear function to encompass the required rotational levels. This gives the required J dependence. To obtain absolute quenching rates, the quenching cross sections are normalized to  $J=0$  and multiplied by the average  $Q_0$  of  $5.6 \times 10^8 \text{ s}^{-1}$  (Ref. 10). This analysis is valid if the rate of quenching from  $v'=1$  is nearly equal to quenching rate from  $v=0$ . This assumption is supported by the work of Copeland, Wise, and Crosley<sup>9</sup> in their measurements of total cross sections for removal from  $v'=1$  by  $H_2O$  at room temperature. Recent results<sup>11</sup> suggest that the J dependence at elevated temperatures may be less pronounced than in the room temperature data. But, this variance is small and we neglect it in favor of the more complete room temperature data set.

The discussion above relates to our ability to determine the relative fluorescence yield between any two OH PLIF data sets. This is critical in forming the ratio to calculate temperature. A separate concern, however, is

our ability to absolutely determine the fluorescence yield for any given line in any given flame. It appears that, in the absence of detailed data in complex hydrocarbon flame environments, the characteristic value we assume for the quenching rate,  $Q_0$ , is probably only valid to within a factor of two or so for any given flame. This places a fundamental limit on our ability to absolutely quantify the concentration from an OH PLIF image.

An additional concern is our ability to relate relative signals within an image to a relative OH distribution. The temperature dependence of the OH signal due to the Boltzmann population fraction was discussed earlier in some detail. The potential variation of the quenching rate across a given image is an additional source of bias in the relative distributions inferred from a PLIF image. Although the available data is sparse (cf., Ref. 12), most studies that have examined the variation in the quenching rate across a flame come to similar conclusions. It appears that, across hydrocarbon and hydrogen flames, the local environment in which OH radicals are likely to be found is rather similar. As a result, the quenching rate varies by about 10 to 50 percent. The largest variations can be expected in the presence of fuel-rich zones. In a typical PLIF image, the fuel rich zone would be on the fuel side of the flame front. From the point of view of overlaying two PLIF images in order to infer temperature, the effect of varying quench rates across the image should be much smaller inasmuch as the spatial variation should be similar for both J levels.

### 2.3.2 NO Fluorescence

The A-X system of NO possesses many strong transitions in the wavelength region near 223 nm. This wavelength regime is accessed by either frequency-doubled excimer-pumped dye lasers or frequency-doubled and -mixed Nd:YAG-pumped dye lasers. Both approaches were used in this work, yielding similar pump energies. Unlike OH, off-diagonal transitions in this system can be as strong, or stronger, than diagonal transitions. Einstein co-efficients for various bands are summarized by Piper and Cowles.<sup>13</sup>



For applications in scattering environments, we again seek an excitation/detection strategy which well separates the laser wavelength from the fluorescence detection wavelengths. An examination of the Franck-Condon matrix, however, quickly reveals several important distinctions in the NO spectrum relative to OH. The (1,0) approach developed for OH suffers from a relatively weak absorption strength and a broadly distributed oscillator strength among transitions with large  $\Delta v$ . This spreads the fluorescence out over nearly 100 nm between 215 and 310 nm. Furthermore, the excitation wavelength (near 215 nm) is inconvenient for both types of pulsed dye lasers.

An alternative approach that excites transitions in the (0,0) band near 225 nm circumvents many of these problems. Firstly, the Franck-Condon matrix is more tightly grouped near the (0,0) band, permitting relatively narrower filtering of the fluorescence and thus minimizing the potential for chemiluminescent interference. Secondly, the absorption transition is stronger than the (1,0) band. Thirdly, the strongest fluorescence bands are actually shifted to the (0,1) and (0,2) bands. Finally, the excitation wavelength is conveniently accessible to both pulsed lasers.

Figures 5 and 6 summarize our excitation/detection strategy for the NO molecule. In Figure 6, the excitation wavelength is denoted by the double-arrow near 225 nm. The vertical arrows represent the various fluorescence bands and their height is scaled according to the relative Einstein A-coefficient. The smooth curve represents the transmission function of the filter combination used in this study. It consists of a 10 nm bandpass filter centered at 253.7 nm (Andover Filter Corporation) and a 2 mm UG-5 glass filter from Schott. The UG-5 provided a long-pass cut-off which decreased the filter transmission at the 225 nm below 0.01 percent. As this figure shows, some of the available fluorescence is lost in the poorly transmitted (0,1) band. Subsequent work with more closely tailored filter transmission functions should permit rather more sensitive detection than in the present work.

The basic approach for NO-based thermometry is identical to that used for OH. The calculation of the fluorescence yield, however, is greatly simplified.

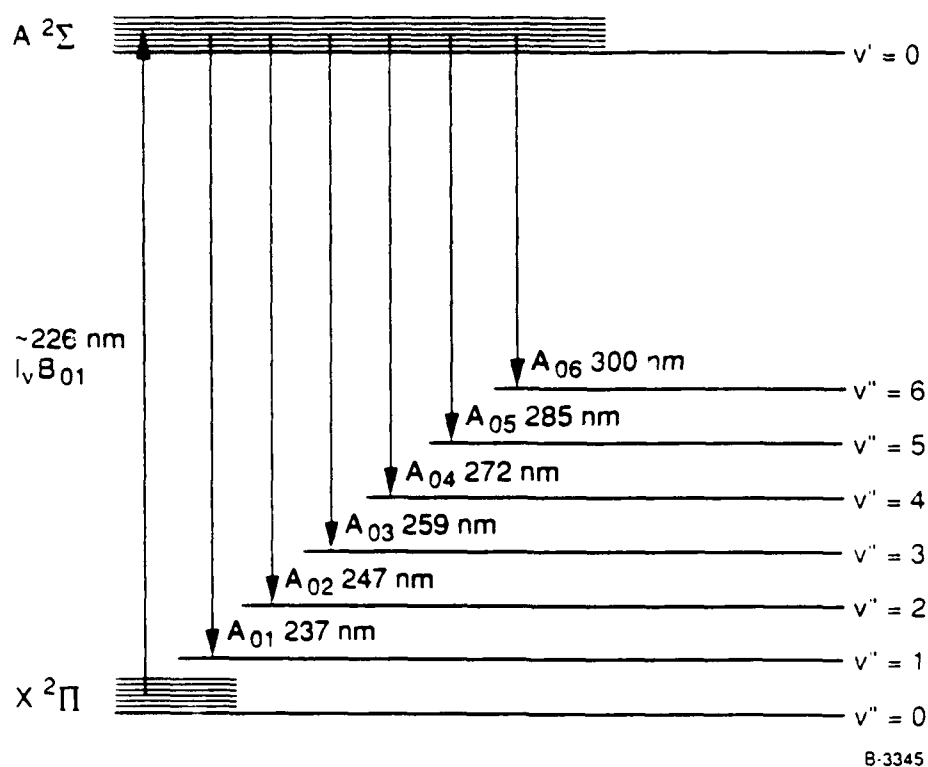


Figure 5. Schematic Energy Level Diagram Showing Important Processes in Laser-Induced NO Fluorescence.

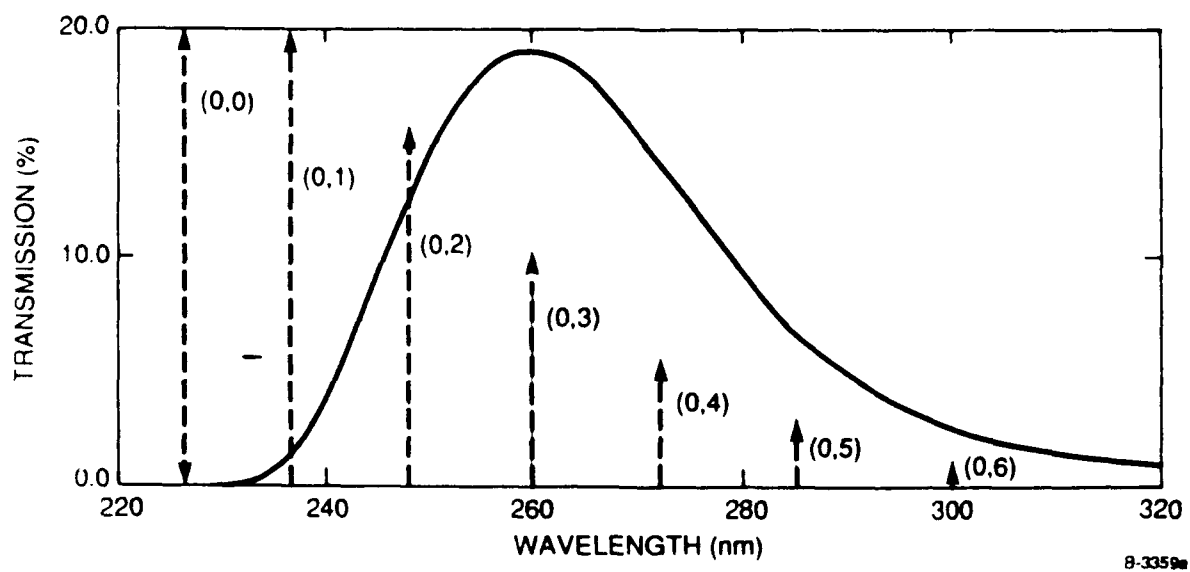


Figure 6. NO Fluorescence Transmission

Since we are exciting  $v'=0$ , we need not consider vibrational energy transfer. Thus, our fluorescence yield reduces to

$$F_y = \frac{A}{A + Q} \quad (10)$$

The situation is further simplified by the observations<sup>14,15</sup> that neither the A coefficients (summed over all available branches) nor the quenching rate is dependent on the J-level excited by the laser. Hence, the ratio of the fluorescence yields for any two J-levels is unity.

Unlike OH, however, no absolute Einstein B coefficients have been tabulated. The B coefficient is given by

$$B = \frac{8 \pi^3}{3h^2 c} \rho \frac{S_{J', J''}}{2J'' + 1} \quad (11)$$

where

$\rho$  = transition matrix element

$S_{J', J''}$  = Honl-London factor.

Thus, the ratio of B-coefficients for two transitions is

$$\frac{B_u}{B_L} = \frac{\rho_u}{\rho_L} \cdot \left( \frac{S_{J', J''}}{2J'' + 1} \right)_u \cdot \left( \frac{2J'' + 1}{S_{J', J''}} \right)_L \quad (12)$$

Because the transition matrix is essentially independent of J, the ratio of B-coefficients reduces to

$$\frac{B_u}{B_L} = \frac{(S_{J', J''})_u}{(S_{J', J''})_L} \cdot \frac{(2J'' + 1)_L}{(2J'' + 1)_u} \quad (13)$$

which is just the ratio of line strengths.

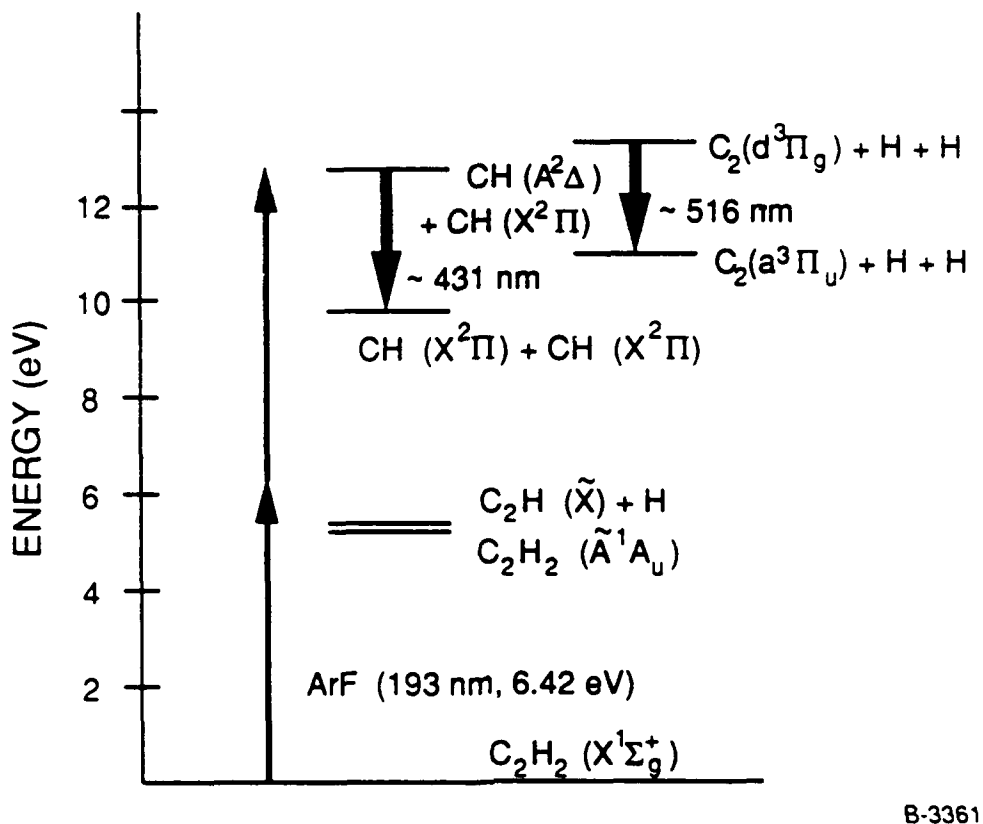
The NO A-X system is best described by Hund's case b for the A state and is intermediate between case a and case b for the X state. Formulas for the line strengths for this type of system are found in Ref. 15 and were used to calculate the relative linestrengths for the isolated transitions used. Term energies were calculated using the formulas of Diecke and Crosswhite<sup>16</sup> with molecular constants of Engleman, et al.<sup>17</sup>

#### 2.4 Multiphoton Photodissociation of C<sub>2</sub>H<sub>2</sub>

Molecules containing three or more atoms become increasingly difficult to detect with fluorescence because transition probabilities are lower than atomic or diatomic species and because the fluorescence tends to be distributed over a quasi-continuum with low spectral intensity. Many hydrocarbon molecules, however, have bond energies between 3 and 6 eV (e.g., H atom abstraction from CH<sub>4</sub> requires ~4.3 eV). Photons with this energy (or greater) may bring a molecule into a state which very rapidly dissociates - a process termed photodissociation. At high photon fluxes, it is possible to further excite the photofragments, leaving them in an electronically excited state which radiatively decays to the ground state of the fragment. Detection of the fluorescence indicates the presence of the parent, dissociating molecule.

A molecule of interest in combustion systems which exhibits such behavior is acetylene (C<sub>2</sub>H<sub>2</sub>). An energy level diagram which includes dissociated states is shown in Figure 7. The higher lying states contain electronically excited CH and C<sub>2</sub> fragments. The vertical arrow represent the energy available from a photon at 193 nm (6.42 eV). The horizontal lines indicate the minimum energy of a particular electronic manifold, each of which contain many rotational and vibrational states of higher energy.

Absorption of a single photon brings the system into a manifold which includes an electronically excited state of acetylene and a dissociated state, C<sub>2</sub>H + H. Absorption of an additional photon by the excited state acetylene brings the system to a dissociated state of CH\* (A<sup>2</sup>Δ) and CH (X<sup>2</sup>Π). The CH\*(A) fragment will decay radiatively and collisionally to the X state, providing a

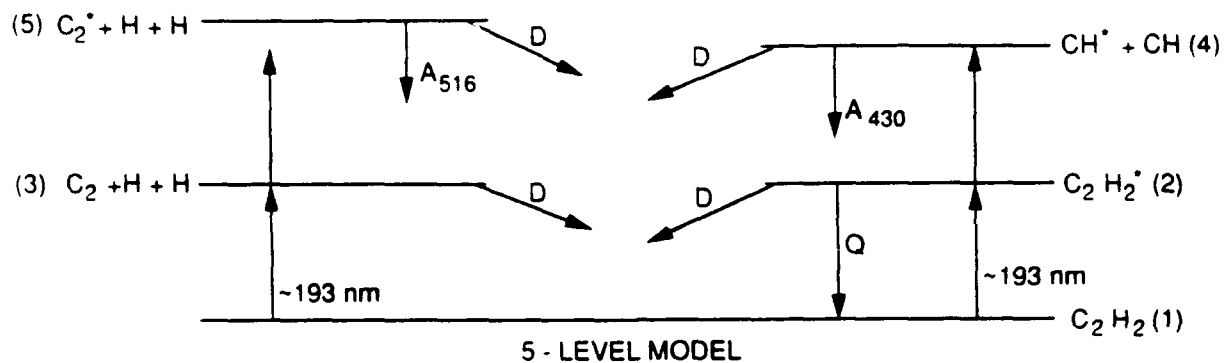


B-3361

Figure 7. Energy Level Diagram Showing Relevant Processes for Multiphoton Photodissociation of Acetylene

detectable fluorescence signal. Absorption of two additional photons by the  $C_2H$  state brings the system to a highly excited dissociated state,  $C_2^* + H$ . Radiative decay of this state provides an additional detection channel. (Further details can be found in Refs. 18 - 20).

A rate equation analysis similar to that used to develop Eq. (1) is required in order to relate the observed signal to the parent molecular concentration. A five-level model is drawn schematically in Figure 8. The processes involved are the same as in the LIF figures except that we have included a channel with rate  $D$  which does not terminate in any levels. This is to allow for collisional and other processes which remove molecules from the system altogether.



8-3358

Figure 8. Diagram of Five-level Photodissociation Model

The number of photons collected through the CH emission channel will be given by

$$S_F = \eta \frac{Q}{4\pi} N_4 A V_c \quad (14)$$

where  $A$  is the spontaneous emission rate for the collected transitions and  $N_4$  is the number density elevated to level 4. Writing rate equations for levels 1-5, assuming steady-state conditions, and solving for  $N_4$  as a function of  $N_1$ , we find

$$S_F = \eta \frac{Q}{4\pi} N_1 A V \frac{A W_{24} W_{12}}{(Q_{21} + D + W_{24} + W_{21})(W_{24} + D)} \quad (15)$$

where

$$W_{ij} = I B_{ij}.$$

This suggests that the signal should be linear with  $N_1$  (i.e., the signal is linear with respect to the acetylene ground state number density) and quadratic in  $I$ . The quadratic dependence on incident power has been observed experimentally.<sup>19</sup>

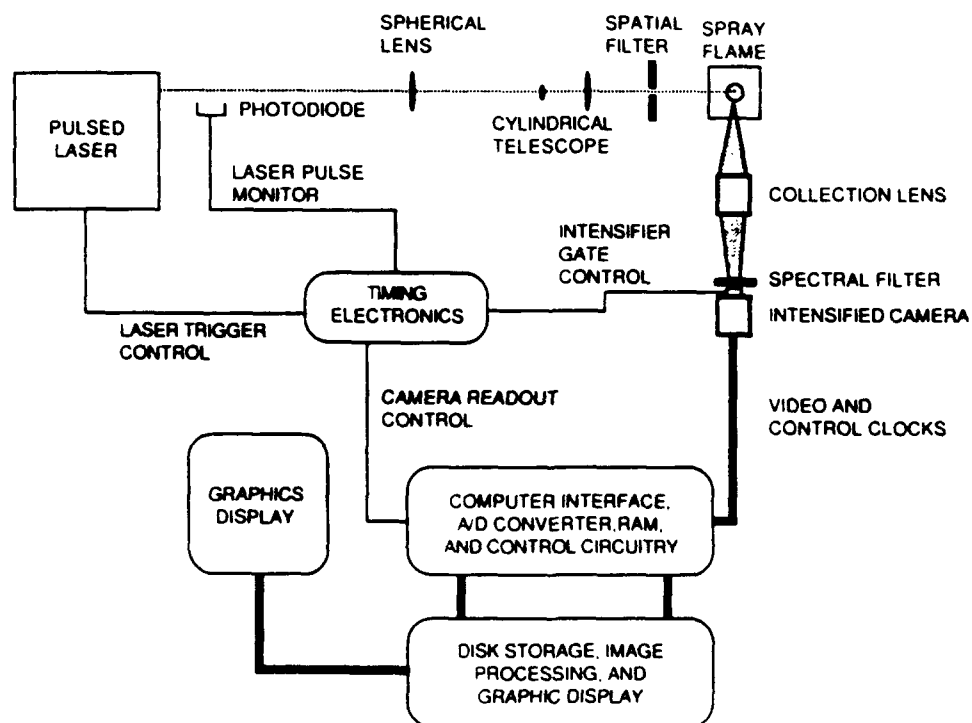
The low-intensity limit invoked in the development of Eq. (1) allows the steady-state, ground-state population to be related to the unperturbed ground state population. However, the existence of additional channels for removing population from the ground state to the bath level links the population in all six levels. Consequently,  $N_1$ , the steady-state population in the ground state acetylene, is not necessarily simply related to the initial acetylene population. Furthermore, it is likely that acetylene itself, or other photo-fragments, are efficient quenchers of intermediates or  $CH^*$ , so that the  $Q$ 's in the denominator of Eq. (15) will exhibit a complicated dependence on  $N_1$ . This is particularly significant in liquid hydrocarbon spray flames where the acetylene mole fractions may approach a few percent.

Many other molecules in a flame environment will absorb 193 nm radiation. Species which will dissociate to yield  $CH^*$  (hence entering our detection channel) include:  $C_2H_6$ ,  $CH_3OH$ , and  $C_2H_5OH$ . Strong absorption will also occur from  $O_2$  and  $H_2O$ , both of which dissociate to radical fragments. Thus, we cannot conclude that this technique is necessarily a quantitative diagnostic for  $C_2H_2$ , although it should serve to detect the presence of acetylene and is thus of utility as a combustion diagnostic since it will mark fuel-rich regions of the flame. In contrast to the OH LIF signal, which provides information in the hot combustion product gases, and the NO LIF signal, which is seeded into the cold spray region, the  $C_2H_2$  provides access to phenomena occurring in the hot, pyrolyzing regions of the flame and should serve to indicate the presence of the reaction zone.

### 3. EXPERIMENTAL SETUP

This section discusses the experimental facilities used to carry out the program. It begins with a discussion of the spray facility fabricated for the program and suggests a simplified model of the physical structure of the flame. The laser systems used for the various PLIF and PMPD experiments are discussed next. Finally, some of the characteristics of the imaging system used to acquire the PLIF data are discussed.

Figure 9 is an overview of the experimental arrangement. A tunable, pulsed laser is used to generate laser radiation at the wavelength of the desired molecular transition. The pulses are typically  $\sim 10$  ns in duration. The light pulse is transformed by a cylindrical Galilean telescope into a sheet typically 5 to 10 cm in height. This sheet (loosely focused by a spherical lens behind the telescope) is directed across the plane of interest in the burner.



A-9980

Figure 9. Schematic Diagram of Typical PLIF Experimental Setup



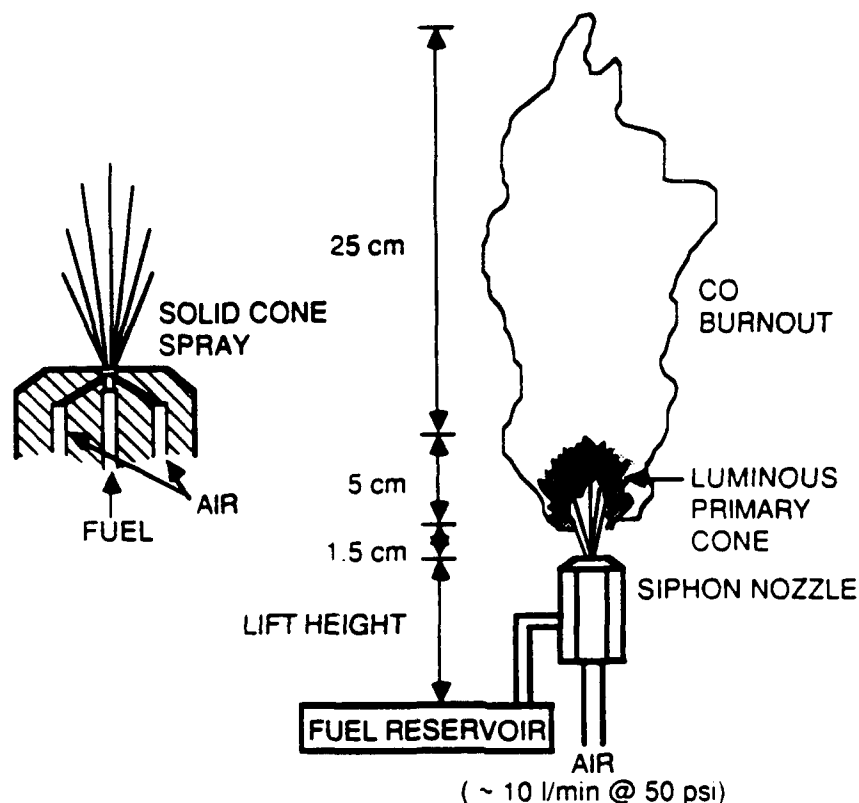
Fluorescence from the laser sheet is imaged at right angles through a collection lens and spectrally filter onto the surface of an intensified CCD-array camera. The intensifier is time-gated to a minimum of about 1  $\mu$ s and the gate is synchronized with the arrival of the laser pulse by a series of timing units. The operation of the camera system, image acquisition, and image processing are all provided by a dedicated personal computer.

### 3.1 Spray Flame Apparatus

The spray flame combustor developed for this program consisted of an air-atomizing siphon nozzle (Delavan model 30609-2) mounted in the center of a 15 x 15 cm duct. Fuel is siphoned from a constant level reservoir and sprayed vertically upward. The bottom of the duct is open to the atmosphere. An exhaust hood above the flame induces a secondary flow through the duct and around the nozzle, providing additional oxidizer and entraining droplets passing around or through the flame. A series of flow straighteners in the duct below the nozzle eliminated large scale structures and transverse motion in the surrounding flow, but no attempt was made to ensure laminar co-flow. The flame was ignited with a propane torch and burned stably over a variety of atomizing air flow rates.

Atomizing air was metered through a rotameter and typically provided at 50 psi. Stable flames were achieved for air flow rates between 15 and 40 lpm (referenced to atmospheric pressure). At lower flow rates, the fuel atomization was poor and the flame sputtered out. At higher flow rates, the flame was blown off the nozzle. The fuel used in this study was n-heptane. A schematic diagram of the nozzle and flame structure is provided in Figure 10.

The air-atomizing nozzle induces a fuel flow by the venturi effect at the nozzle orifice. It is capable of fuel flow rates as low as 20 ml/min and thus suitable for bench-top experiments. The fuel flows along a central tube with the primary (atomizing) air flow slightly swirled at the periphery. The shear between the exiting fuel and air flows atomizes the fuel jet, producing a solid cone spray.



8-3362

Figure 10. Schematic Diagram of Spray Flame Apparatus

The droplet size distribution of the spray depends on the height through which the fuel must be lifted, the atomizing air flow rate, and characteristics of the fuel such as surface tension and viscosity. No attempts were made to measure the droplet size distribution, although data provided by the manufacturer suggested the Sauter mean diameter of the fuel spray was on the order of  $50 \mu\text{m}$  and the maximum droplet diameters on the order of  $100 \mu\text{m}$ . Variations in flow conditions alter these numbers somewhat, but they may be taken as representative.

The fuel flow rate was not metered, but based on nominal air flow rates and manufacturer data, we estimate that the overall stoichiometry of the burner is near unity. Typical flow velocities near the primary flame zone are on the order of a few hundred cm/s. For reference, the laminar flame speed for stoichiometric heptane/air mixtures is 42 cm/s and the adiabatic flame temperature is 2200 K.<sup>21</sup>

Photographic surveys of the flame structure were carried out initially to establish the stable operating envelope and to characterize the gross physical environment. The droplet spatial distribution within the cold and burning spray was visualized by focussing a thin sheet of visible wavelength laser light across the centerline of the spray and imaging the elastic scattering from the droplets at right angles with a film camera. For burning sprays, the flame emission was also integrated on the film plane. Examples of these data have been forwarded previously under separate cover in month 3 of the program.

An example of the instantaneous droplet distribution in a cold spray is shown in the photograph of Figure 11. The image is of a single laser pulse so that the droplet distribution is frozen in time. The rich spatial structure within the fuel spray is clearly evident. Co-addition of multiple laser shots on the film plane averaged this structure and resulted in the typical solid cone spray pattern. The instantaneous photograph in Figure 11, however, reveals that the "solid-cone" spray is in fact made up of a complex series of



Figure 11. Photograph of Instantaneous Droplet Spatial Distribution in Cold Spray

regions containing few droplets separated by filaments containing a much higher droplet density. These structures, formed near the jet exit, persist far downstream. This marked difference between mean and instantaneous spatial structures is also revealed in the species and temperature images discussed in Section 4.

Similar photographs obtained under burning conditions showed that the central core, to a height of about 5 cm, was largely unaffected by the presence of the flame, excepting a gradual decrease in the apparent droplet density. Beyond this point, the droplet density fell quickly. A substantial number of droplets could also be seen completely outside the flame. Some droplets may have enough momentum to pass through the flame zone unevaporated. Furthermore, the volumetric expansion of the hot combustion gases acts like a bluff-body above the spray, deflecting streamlines around the flame.

No direct simulations of the chemical structure of the flame incorporating finite rate kinetics exist. Probe measurements of stable species mean profiles have been made by many groups (*cf.*, Ref. 22) and we may draw upon these to build a qualitative understanding of the chemical structure of the flame. The present flowfield, of course, is turbulent and the high temporal resolution of the PLIF technique will permit instantaneous sampling of spatial structure in the species concentration fields. Hence, the observations of mean structure will have only limited applicability in interpretation and understanding of the PLIF species images.

The central core of the flame consists of a droplet laden zone where the heptane droplets evaporate. Because the inner cone is relatively fuel-rich, the heptane vapor first pyrolyzes to smaller hydrocarbons before significant conversion to CO and H<sub>2</sub>O occurs. As in partially premixed gaseous flames, we can expect a rather thin zone separating the combustion products from the reactants (here reactants are understood to include pyrolysis products such as methane, acetylene, and other light hydrocarbons). This reaction zone will be characterized by the bright blue-green color from CH<sup>\*</sup> and C<sub>2</sub><sup>\*</sup> emission. Beyond this reaction zone, stable high-temperature products such as OH and CO will

form in significant densities. Further downstream, the OH will oxidize the CO to form  $\text{CO}_2$  and  $\text{H}_2\text{O}$ . In summary, we expect to find pyrolytic species in the central core near the flame zone and product species such as OH beyond this flame zone.

Although no turbulence characterization experiments were attempted in this program, we can estimate typical order-of-magnitude levels and relate them to the gross phenomena of the flame structure. Near blow-off, the volumetric air flow rate through the nozzle is on the order of 32 lpm. The flame at this point typically stabilizes about 1 to 2 cm above the orifice, where the jet cross-sectional area is on the order of  $1 \text{ cm}^2$ . Hence the nominal mean velocity is on the order of 500 cm/s. If we assume a modest turbulence intensity ( $u'/u$ ) of 10%, then the eddy turnover velocity is on the order of 50 cm/s. Interestingly, this is on the order of the laminar flame velocity for this system. This suggests that as we approach blowoff, the typical velocity fluctuation may exceed the propagation speed of the flame, hence, preventing stable attachment in the shear layer at the jet periphery.

### 3.2 Laser Systems

Three laser systems were employed during the course of this work. The primary source was a Nd:YAG-based system consisting of a Spectra-Physics DCR-4 YAG laser pumping a PDL-2 dye laser with capability for frequency-doubling and frequency-mixing. For the OH measurements, pulse energies on the order of 25 mJ were generated in the vicinity of 283 nm by frequency-doubling Rhodamine 590 dye. For the NO measurements, it was necessary to mix this doubled output with residual infrared at  $1.06 \mu\text{m}$  to generate radiation near 225 nm. By optimizing a dye mix of Rhodamine 590 and Rhodamine 610, pulse energies on the order of 5 to 8 mJ were obtained.

Additional NO measurements were made using an excimer-based system consisting of Lambda-Physik LPX 210i excimer laser operating with XeCL pumping a Fl 3002 dye laser with capability for frequency-doubling. Pulse energies on

the order of 2 mJ were generated in the vicinity of 225 nm using BBO doubling of LC4500 dye.

For the  $C_2H_2$  photodissociation measurements, a Questek 2820 excimer laser operating with ArF at 193 nm was used. Typical pulse energies measured at the laser exit were ~250 mJ.

### 3.3 Imaging Detector System

The core of the imaging system used in this program is a PSI-designed and built intensified CCD array camera. The CCD is a model NXA 1060, provided by Amperex along with printed circuit boards to control the array readout and pre-processing functions. This is a state-of-the-art imaging array combining low noise, a wide linear dynamic range ( $> 40$  dB), and compact packaging. A PSI-designed camera and controller was built around this chip. An ITT Model 4111 single micro-channel plate intensifier tube is coupled to the front of the array used a 2-1 fiber-optic minifier. The intensifier controller was also designed and fabricated at PSI.

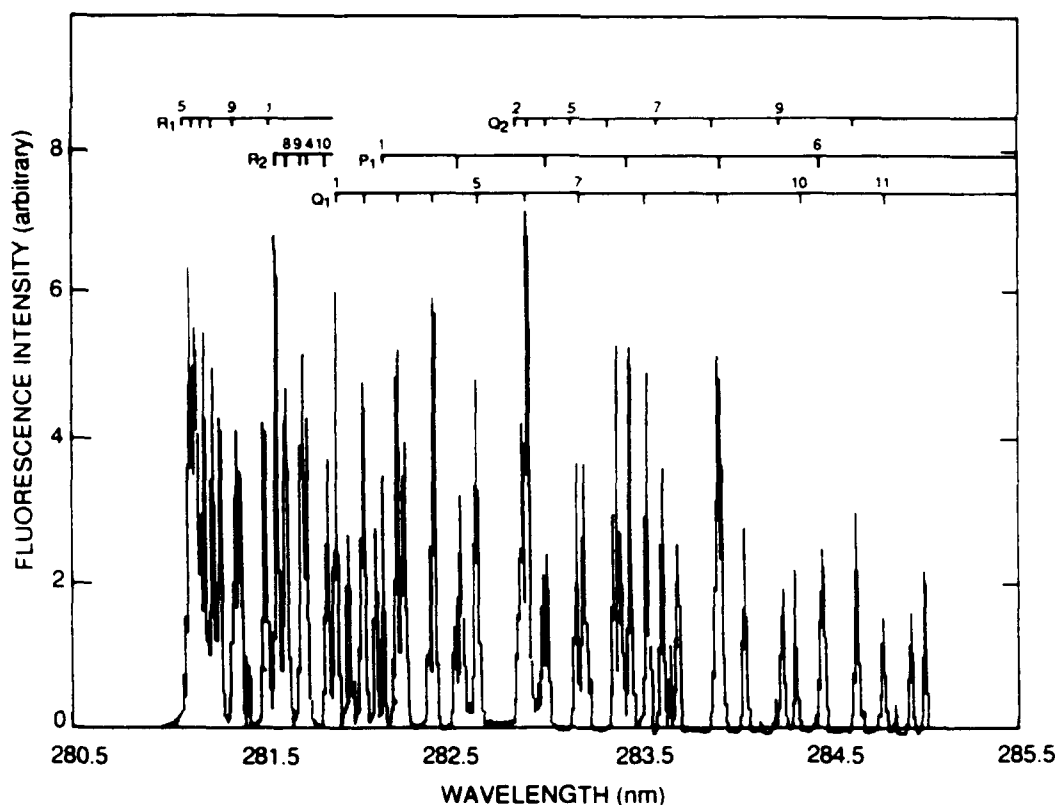
The CCD provides 512 x 240 resolution per frame with a maximum frame repetition rate of 60 Hz. The video signal is digitized and formatted by a Data Translation model 2853 frame grabber housed in a Compaq Model 286 personal computer. Custom software was developed which permits asynchronous control of the camera and synchronization with the pulsed laser systems. The intensifier is gated on coincidentally with the laser pulse in order to eliminate unwanted background light interference. The camera system is calibrated against a known responsivity detector so that at any gain level, it is possible to relate the A/D level of a pixel in the digital image to a number of incident photons.

#### 4. RESULTS AND DISCUSSION

This section presents representative results from the species and temperature imaging experiments. Unfortunately, limitations of black and white printing reduce the apparent content of information in the figures shown. False color encoding of the digital information is vastly superior and aids image interpretation. Color images of the data are available from the authors.

##### 4.1 OH and OH-Based Temperature Results

Prior to PLIF experiments in the spray flame, the dye laser was wavelength-calibrated against the OH absorption spectrum by scanning through the appropriate wavelength regime and recording the fluorescence at a single point in the post-combustion gases of a methane-air Bunsen burner. A portion of such an excitation spectrum is shown in Figure 12 with the appropriate line



B-1797

Figure 12. A Partial Excitation Spectrum of the (1,0) Band of the OH A-X System

assignments. Using the analysis of Subsection 2.2, several isolated peaks in this spectrum were plotted against the rotational energy of the laser-excited level to check the validity of the fluorescence yield model. These results are shown in Figure 13, where the data are fitted to a straight line. The temperature inferred from the slope of this line is  $1843 \pm 300$  K. A radiation corrected thermocouple measurement (13%Rh/Pt-Pt, 0.003 in. bead) at the same flame location determined a temperature of 1847 K. Although the apparent close agreement must be considered to be at least somewhat fortuitous, this result suggests that our fluorescence modelling approach is sound.

An example of an OH PLIF measurement is shown in Figure 14. The field of view is the central  $6 \times 4.5$  cm plane of the burning spray. The bottom of the image corresponds to the flame stabilization zone, approximately 1 cm above the nozzle exit orifice. The data are grouped into 10 gray scales with increasing darkness indicating higher photon fluxes. The gray scale is shown at the bottom of the image for reference.

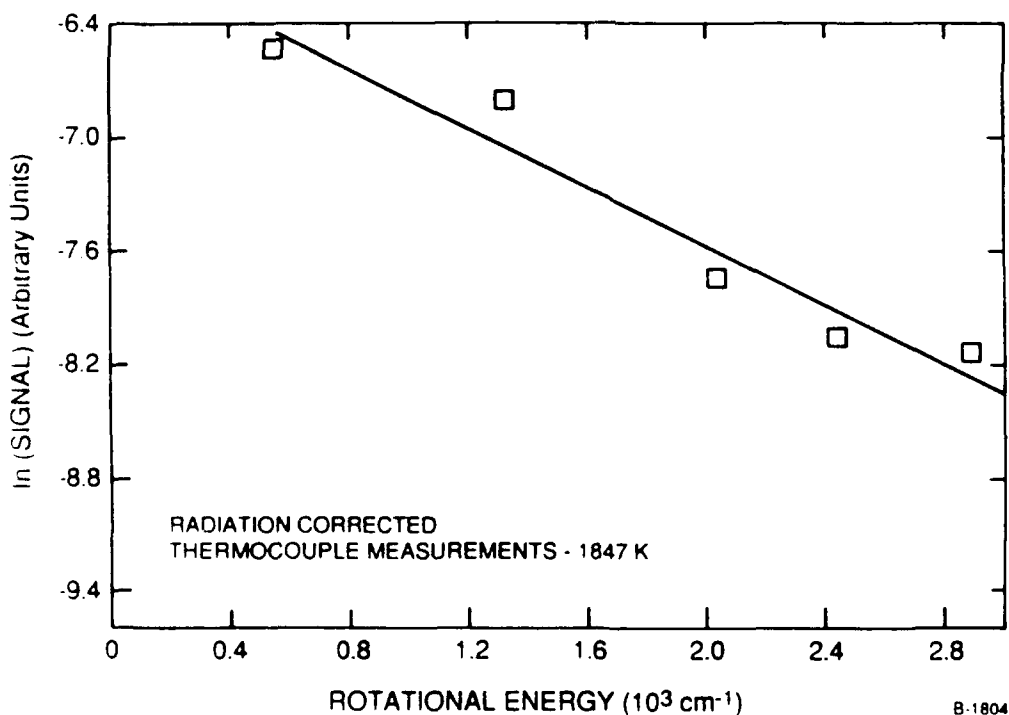


Figure 13. A Boltzmann Plot of the Peak Fluorescence from Several Isolated Lines in the Spectrum of Figure 12



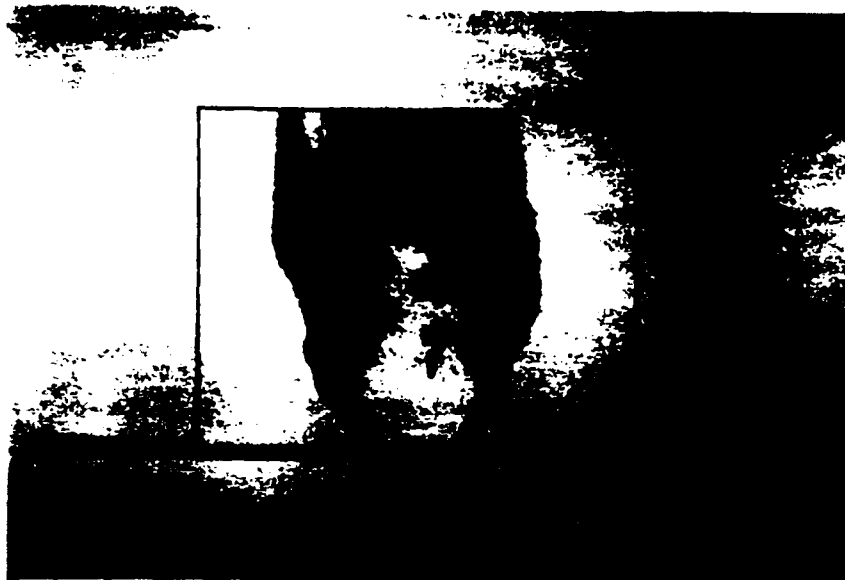


Figure 14. OH PLIF Image in Central Plane of Spray Flame

The image is a single laser shot exciting the  $Q_1(5)$  transition at 282.67 nm. This transition is a weak function of temperature (see discussion in Subsection 2.3), so the fluorescence distribution may be considered to reflect the relative OH number density across the field of view. From our calibrations, we estimate that the peak signal levels in this image correspond to about 3800 photons per pixel. Using Eq. (1) and assuming a nominal temperature of 2000 K, this corresponds to a peak concentration of  $5 \times 10^{15} \text{ cm}^{-3}$ . The shot-noise limited signal to noise ratio is given by

$$\text{SNR} = \sqrt{q S_F} \quad (16)$$

where  $q$  = quantum efficiency at detected wavelength.

For nominal 10 percent quantum efficiency,  $\text{SNR} \sim 20$ . The concentration which generates a signal equivalent to the noise level is thus  $2 \times 10^{14} \text{ cm}^{-3}$ .

The intensified camera system is sufficiently sensitive to be considered a quantum-limited detector. That is to say that sufficient gain is available to digitize a single detected photon. For 10 percent quantum efficiency at the intensifier photocathode, this corresponds to 10 incident photons, which in turn corresponds to a minimum detection threshold on the order of  $10^{13} \text{ cm}^{-3}$ . The signal to noise ratio at this limit is unity.

The image reflects several interesting features of the burning spray. Note first that there is no signal in the central core of the flame. This is the cold evaporating/pyrolyzing spray and we expect no OH to be present here. The lack of signal indicates that we efficiently discriminate against the elastic scattering of the laser light despite the fact that it is several orders of magnitude stronger than the fluorescence light. Surrounding this core near the bottom of the image is a reacting sheath, stabilized at the instantaneous position where sufficient droplet evaporation has occurred to permit burning. The sheath is nominally the same on both sides of the core which indicates that scattering or absorption of the laser beam energy is also not a problem, even in the high droplet density region near the image bottom.

Along the image centerline but higher in the flow is revealed a complex pattern of burnt gas (regions containing high OH concentrations) and unburnt gas. The turbulence of the flame is evidently of sufficient intensity to separate the flame zone and develop isolated packets of burning gases. Examination of hundreds of similar images support this conclusion and dramatically illustrate the complex nature of the instantaneous flame structure.

A single point probe with continuous time resolution would record a time-varying signal which could not be reconstructed to yield the spatial information present in even a single PLIF image. Indeed, as will be demonstrated in the following sections, the temporal average value at any given point in the flow appears to be determined more by the intermittency of packets containing either nearly uniform high levels of OH or no OH, than by the existence of any mean value lying between these two extremes. This conclusion

is partially supported by conditionally sampled OH and mixture fraction data in a turbulent hydrogen-air diffusion flame,<sup>12</sup> where over a wide range of mixture fractions, the OH concentrations varies by only an order of magnitude.

Because only one camera/laser combination was available for this work, it was not possible to ratio two simultaneously acquired OH images excited from different transitions. Instead, 256 instantaneous OH images from  $Q_1(5)$  excitation were averaged together to yield a "mean" OH distribution. Then, the laser was tuned to the  $Q_1(12)$  transition at 285.3 nm and the processes was repeated. Each image was corrected for the average vertical variation in the laser sheet energy distribution. The images were then ratioed according the theory developed in section 2.2 to yield a map of the "mean" temperature distribution. This temperature image is shown in Figure 15 where the data are mapped onto the gray scale with a range from 1300 K to 2100 K.

Several issues are involved in the description of the spatial distribution of the temperature in Figure 15. A distinct left/right asymmetry is apparent, with the right side of the flame appearing about 10 percent hotter than the

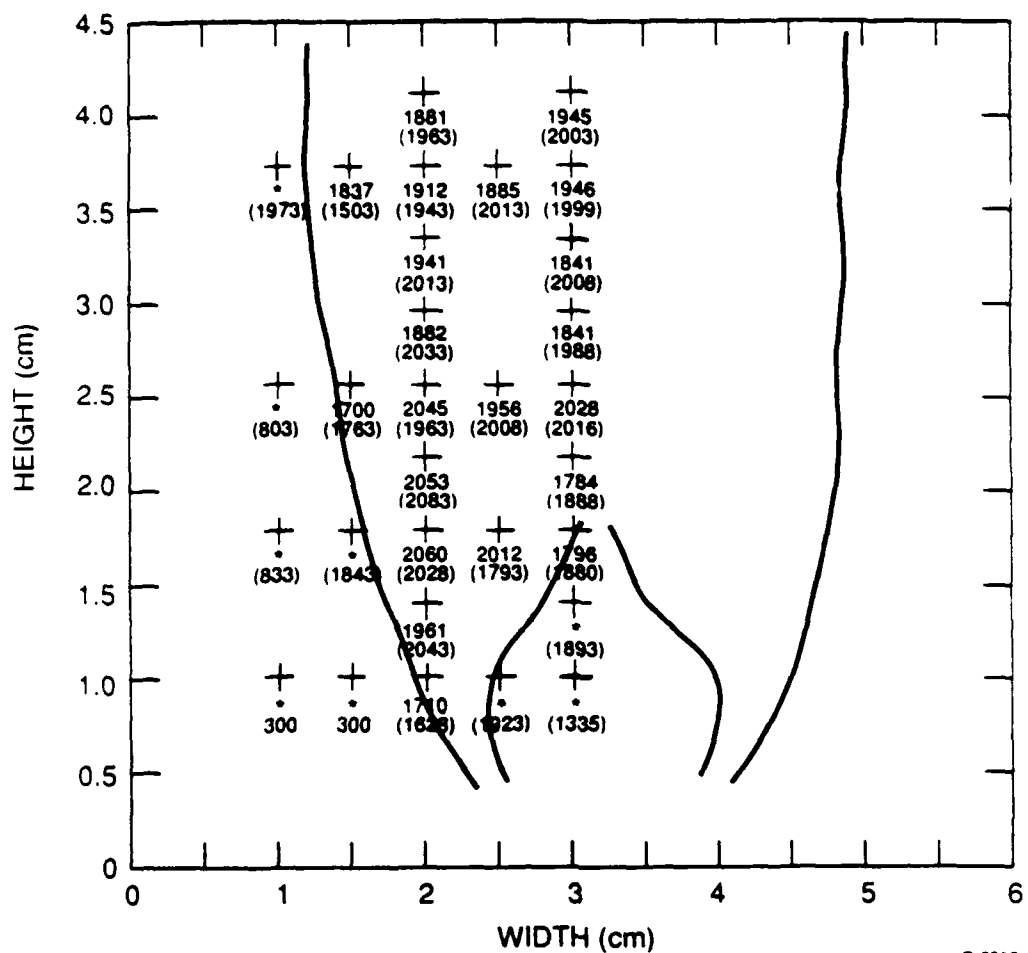


Figure 15. Temperature Image Inferred From the Ratio of  $Q_1(5)$  Excitation and  $Q_1(12)$  Excitation in OH

left side. This is reflected in the concentration images used to infer the temperature. It results from excessive absorption of the laser beam on the  $Q_1(5)$  transition as it propagates from left to right across the image. Although not apparent in the instantaneous images, the 256 frame average revealed that the mean distribution was about 25 percent less on the right side of the image than the left. This level of attenuation was not evidenced in the corresponding image from the  $Q_1(12)$  transition. Hence, the temperature calculation algorithm deduced a relatively higher temperature on this side of the flame. The obvious solution to this problem is to simply choose a weaker branch for monitoring the low-J population. An excellent candidate for this would be the  $P_1(4)$  transition at 283.5 nm which has less than 60 percent of the strength of the  $Q_1(5)$  transition and somewhat lower population. Preliminary images of distributions from  $P_1(4)$  excitation show no attenuation.

Secondly, it should be reiterated that the edges of the temperature map do not correspond to sudden changes in the temperature field. Rather, they correspond to regions where the OH number density falls below our ability to detect it, thus precluding a temperature determination. This reflects the fact that our temperature measurement is conditioned on the presence of OH concentrations greater than about  $5 \times 10^{14} \text{ cm}^{-3}$ . Much of the remaining small scale structure present in the region immediately above the spray cone we attribute to insufficient averaging. The spatial distribution of these residual structures suggest that they are related to the distribution of turbulent fluctuations in the flame itself.

As a means of comparison, several thermocouple traverses were performed in the flame. The thermocouple used was 13 percent Rh/Pt-Pt with a 0.005 in. bead. For this small bead, radiation corrections based on a Nusselt number of two were generally on the order of 80 K. Because the spatial position of the thermocouple relative to the image could not reasonably be determined to the precision of a pixel dimension, the PLIF data was averaged in a 5 by 5 pixel box around the nominal location of the corresponding thermocouple data point. The summary of this comparison is shown in Figure 16. The crosses represent the comparison points with the thermocouple data shown below in parentheses.



B-2902a

\* Indicates [OH] below detection thresholds

Figure 16. Comparison Between PLIF and Thermocouple Temperature Determinations

The outline of the PLIF temperature map is drawn for reference (note that the spatial scale is different in the horizontal and vertical directions). The asterick indicates regions where the OH density was too low to permit temperature determination.

Near the spray core, the thermocouple measurements are almost certainly unreliable due to presence of impinging fuel droplets. Because of the laser attenuation problem, we only compared data on one side of the flame. Throughout most of the flame, the agreement with the PLIF measurements is quite good. The discrepancy is typically less than 100 K - the order of the radiation correction. Even the relatively hot region in the middle left of the PLIF

image is picked up by the thermocouple. This first experiment is a strong confirmation of the overall validity of the approach.

Unfortunately, the data set is limited and it is difficult to draw firm conclusion regarding the ultimate accuracy of the technique. Subsequent study should endeavor to examine alternative line pairs and build a statistically significant set of temperature maps over a range of flame conditions in order to thoroughly assess the accuracy of the technique.

A better approach would be to take instantaneous pairs of data, using two lasers and two cameras, and determine instantaneous temperature distributions. Weber and Garscadden<sup>23</sup> have observed that significant temperature errors can occur by inferring temperature from averaged Boltzmann populations in the presence of temperature fluctuations. While our temperature fluctuations are less than they consider and strongly conditionally sampled by the presence of OH, we may incur an upward bias in our inferred temperature using the approach for the present study. Instantaneous population comparisons, however, can be made essentially free of this bias in the presence of Gaussian-distributed fluctuations by choosing the levels so that  $\Delta E \sim 2 kT$ . The fluctuations in the present experiment (and, indeed, in most practical systems) will not be Gaussian so it would be of interest to compare temperature determinations using several line pairs in order to detect any systematic bias scaling with the ratio  $\Delta E/kT$ .

#### 4.2 NO and NO-Based Temperature Measurements

As we expected, we were unable to detect any PLIF signals emanating from nascent NO in the spray flame. The peak temperatures in this flow are too low to promote significant NO formation. Our primary goal, however, was to seed NO into the atomizing air stream and use NO PLIF in this region to determine temperature in the colder regions of the pyrolyzing spray where the OH signal levels were below detection limits. Additionally the NO, which is consumed by the high temperature gases near the flame front, should prove a qualitative

marker of the spatial distribution of low temperature, fuel-bearing zones in the flame.

To this end, approximately 1 percent by volume NO was seeded into the primary atomizing air stream, corresponding to approximately  $10^{17}$  cm<sup>-3</sup> peak concentrations. An example of an instantaneous NO image obtained using the frequency-doubled output of the excimer-pumped dye laser is shown in the left panel of Figure 17. The laser was tuned to 226.4 nm, corresponding to the Q<sub>2</sub>(14) transition where approximately 3 mJ of pulse energy was obtained. The field of view is 4 cm x 3 cm with the concentration range of  $10^{17}$  to  $10^{15}$  cm<sup>-3</sup> mapped according to the gray scale shown, as before.

Using the model developed in Subsection 2.1, we estimate that the peak signal levels correspond to approximately  $4 \times 10^{17}$  cm<sup>-3</sup> of NO, in excellent agreement with our measured flow rates. The maximum shot-noise-limited signal to noise in the left image is about 20 to 1 (3600 photons per pixel). Our ultimate detection limit is, again, the level which generates approximately 10 photons, or  $10^{15}$  cm<sup>-3</sup>. The right panel is the average of 72 such instantaneous frames.

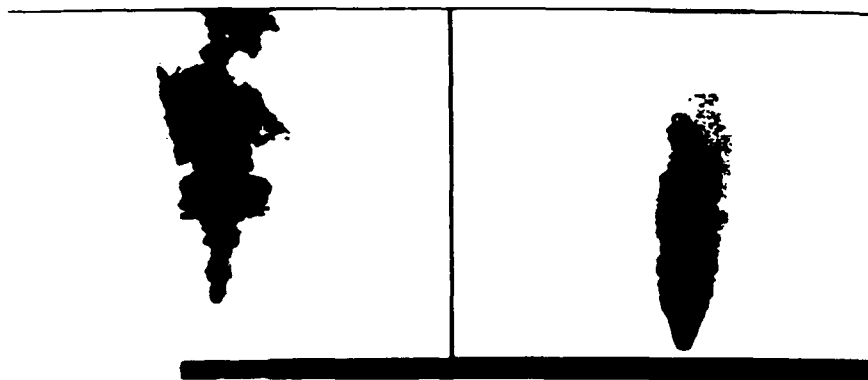


Figure 17. Instantaneous and Average Distributions of NO Seeded Into the Primary Air Stream of the Spray Flame

The difference between the instantaneous and average distributions is striking. The arguments developed above in connection with the OH image are even more strongly suggested by these pairs of images. It would appear that the gradual decay of the NO (in effect tracing the decay of the parent fuel molecule) in the average image is due entirely to intermittency between packets containing nominally unmixed primary air and packets containing essentially no primary air. The predominance of persistent, large scale features in controlling mixing of reacting streams has also been noted by Mungal.<sup>24</sup> This comparison is an archetypal example of the fundamental information available from PLIF imaging techniques which is not possible to obtain with conventional single point techniques.

These NO images provide the severest test for the possible influence of the droplets on the PLIF data since they are obtained in the region of the highest droplet density. The possibility of elastic scattering interference in the detection system was eliminated by noting the the signal completely disappeared between absorption lines. The possible influence of beam distortion is shown to be negligible in Figure 18, which compares NO PLIF images in a non-burning flow with the fuel droplets present (right image) and

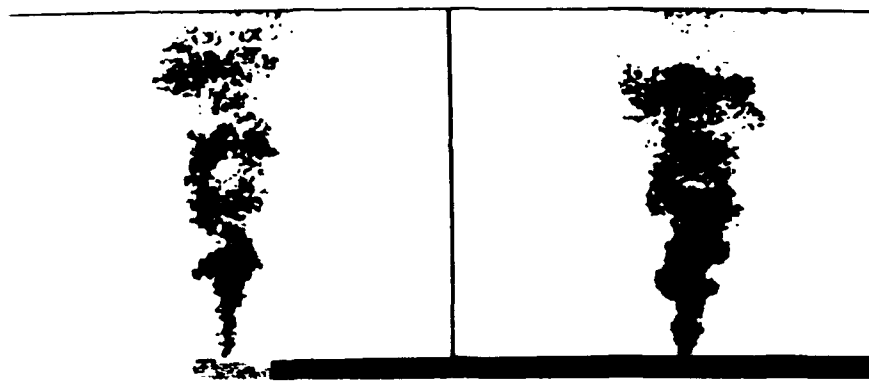


Figure 18. Comparison of NO PLIF Images in Non-Burning Jets With (right) and Without (left) Droplets



with the fuel droplets absent (left image). The only apparent difference between these two images (other than the expected small scale differences due to turbulence) is the slightly increased spreading rate of the jet with droplets present. This is understood by considering that a portion of the available air jet momentum is used to siphon and disperse the fuel stream. Hence, the image on the right, taken with the same volumetric air flow rate, has less initial momentum than the image on the left and spreads more quickly.

Attempts to infer mean temperature distributions in both burning and non-burning spray flames were made using several line pair combinations. An example of a temperature image using the averaged (72 frames) distribution of the  $J'' = 13.5$  ( $Q_1(14)$  line) and  $J'' = 26.5$  ( $Q_2(26)$  line) in a burning spray is shown in Figure 19. The upper left image is the  $J'' = 13.5$  distribution, the upper right image is the  $J'' = 26.5$  distribution, and the bottom image is the temperature distribution inferred from these two PLIF images. As expected, the high  $J$  distribution persists further downstream into the higher temperature region of the flow. The temperature data is mapped onto a linear range from 300 K to 1100 K.

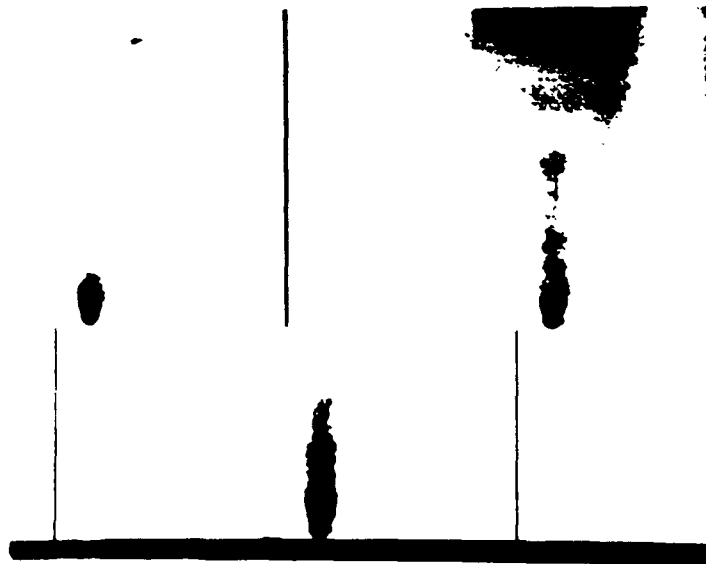


Figure 19. Temperature Determination From NO PLIF

The minimum temperature near the jet exit orifice should be on the order of 300 K since no appreciable heating of the gases would be expected to have occurred there. In the image shown, the minimum temperature is about 450 K. This preliminary data set does not correctly recover the absolute temperature, but since the spatial distribution of temperature is reasonable, the discrepancy suggests a systematic error in our approach.

There are several possible explanations for this error. Although our fluorescence yield model is supported by several experimental observations, it is possible that the relatively high NO concentrations used give rise to a self-quenching effect not considered. The model developed in Subsection 2.3 is not based on any experimental determinations of the rate of NO self-quenching. There may be a J-dependence in the self-quenching which we did not include.

Saturation effects at pulse energies of  $\sim 2$  mJ have been noted by Hanson.<sup>25</sup> Saturation effects should become evident if

$$I_v(B_{12} + B_{21}) \geq Q \quad (17)$$

where, for both transitions  $B_{12} = 1/2 B_{21} \sim 2 \times 10^5 \text{ cm}^2\text{erg}^{-1}\text{s}^{-1}$ . For nominally 5 mJ in a  $5 \times 0.1$  cm sheet with a spectral bandwidth of  $1.0 \text{ cm}^{-1}$ , the spectral intensity,  $I_v$ , is on the order of  $350 \text{ erg cm}^2\text{s}^{-1}$ . For nominal rotational energy transfer rates on the order of  $10^9 \text{ s}^{-1}$ , we find the the stimulated absorption and emission rates are about an order of magnitude less than the quench rate:

$$I_v(B_{12} + B_{21}) \sim 2 \times 10^8 \text{ s}^{-1} \quad (18)$$

Hence, saturation does not appear likely.

A final possibility is a loss of relative gain calibration in our intensifier controller. Preliminary checks of the gain voltage as a function of controller setting appear to confirm our earlier gain calibration. However,

the high J data is obtained with both camera and intensifier gains near their maximum. It is possible that this data is outside the linear response range of the camera system. A check of this would be to use a J value lower than 26.5 for the upper rotational level measurement in order to obtain a higher signal level and permit use of lower system gains. As in the case of the OH temperature measurements, a much larger data base is required in order to confidently assess the quantitateness of the technique.

#### 4.3 C<sub>2</sub>H<sub>2</sub> Measurements

Images of the CH\* emission channel of the acetylene photodissociation were obtained in the burning spray at two magnifications. An example of the signal distribution over a 5.4 x 4 cm field of view is shown in Figure 20. As in the OH image, the bottom of the image corresponds to the stabilization point of the flame, approximately 1 cm above the nozzle orifice. The image exhibits a left to right asymmetry which is due to absorption of the ArF laser sheet by acetylene, other hydrocarbon intermediates, O<sub>2</sub>, and H<sub>2</sub>O. Because the photodissociation signal is proportional to the square of the incident intensity, the relatively modest laser attenuation is accentuated in the image.

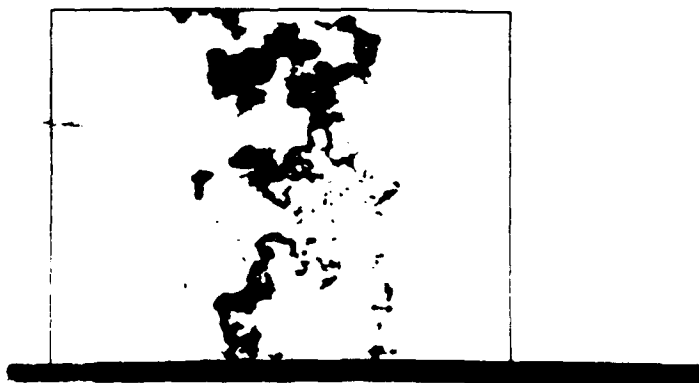


Figure 20. Acetylene Photodissociation Image

The spatial distribution of the signal is consistent with origination from a hydrocarbon pyrolysis intermediate. Note that there is no signal in the lower regions of the inner spray cone. This cold region has not yet generated significant pyrolysis products (no signal was observed in cold heptane sprays). Moving downstream toward the flame zone, the signal increases and reaches a maximum in a relatively thin region then drops off quickly. The interpretation of the photodissociation signal as arising from a gradually increasing concentration of pyrolysis products (chiefly  $C_2H_2$ ), peaking in the reaction zone, and then disappearing is corroborated in this image. Interestingly, isolated packets of high signal can be seen above the central core, suggesting regions where fuel-rich zones (perhaps containing droplets) are burning in isolation from the main reaction zone.

Also noticeable in this image is a thin strand of signal at the left periphery of the flame. This presumably arises from the evaporation of the small number of droplets which pass through the flame zone. The evaporated fuel vapor is entrained into the jet and pyrolyzes as it encounters the product gases at the flame periphery.

Details of the reaction zone structure at the tip of the primary spray cone can be examined in more detail by imaging a smaller region in this vicinity. Figure 21 is an example of the photodissociation signal in a 2.7 cm by 2 cm field of view at the tip of the primary spray region - the zone of maximum flame wrinkling. For this image, each pixel views a region  $83 \times 55 \mu m$ . The fine structure associated with the instantaneous flame front are clearly revealed. The thickness of the bright filaments in this image is on the order of 10 pixels, or about  $600 \mu m$ .

It is interesting to compare the thickness of this zone to the expected laminar flame thickness. The laminar flame thickness can be estimated using the formula<sup>26</sup>

$$L_F \approx S_L / RR \quad (19)$$



Figure 21. PMPD Image of the Detailed Reaction Zone Structure Near the Vicinity of the Primary Flame Zone

where  $RR$  is the global reaction rate and  $S_L$  is the laminar flame speed. The global reaction rate is related to the laminar flame speed by

$$S_L \approx (\alpha RR)^{1/2} \quad (20)$$

where  $\alpha$  is the thermal diffusivity of the gas mixture. For unity Prandtl number, the gas kinematic viscosity,  $\nu$ , can replace  $\alpha$  and we derive that

$$L_F \approx \nu / S_L$$

Taking the kinematic viscosity to be equal to that of air at 1800 K and replacing  $S_L$  with  $40 \text{ cm s}^{-1}$ , we find the expected laminar flame thickness to be on the order of  $500 \text{ }\mu\text{m}$ . This suggests that, for this partially premixed flame, the photodissociation technique can resolve the instantaneous flame zone in this turbulent reacting flow.

Even as a purely qualitative marker of the position and spatial distribution of the reaction zone, the photodissociation signal has merit. Many emerging theories of turbulent reacting flow problems such as blow-off and turbulent flame speed prediction are being developed using the geometrical nature of the flame front (cf., Ref. 27). The photodissociation technique demonstrated here may prove useful in experimental studies of these theories.

## 5. CONCLUSION AND RECOMMENDATIONS

The results of this successful Phase I SBIR program have demonstrated the ability to obtain a variety of instantaneous and mean species distributions in liquid-fueled spray flames. Representative data have been presented for nascent OH distributions, NO distributions seeded into the atomizing air stream, and  $C_2H_2$  or other hydrocarbon distributions. The presence of a moderately dense liquid spray in the measurement volume proved not to be a barrier in obtaining these results.

Using averaged distributions of OH rotational level populations, two-dimensional temperature imaging was also demonstrated. Extension of this technique to instantaneous temperature distributions is clearly straightforward and represents a large step forward in experimental technique for two-phase reacting flowfields. A similar temperature imaging approach based on NO rotational level populations was investigated with a goal of measurements in the colder, evaporating and pyrolyzing region of the spray. While the distribution of temperature in these results appeared accurate, the absolute level requires further work. Several improvements to the experimental technique designed to overcome problems in this initial attempt were suggested.

Regarding the temperature technique demonstrated in this program, it appears that the basic approach is sound. A logical next step in the development and application of the approach is the development of a statistically significant data set, incorporating various transition pairs in similar flames and then investigating any possible effects due to changing flame environments. The extension to instantaneous temperature mapping using two lasers and two cameras is important as well, since it circumvents a systematic source of error accrued by taking the ratio of averaged rotational populations in the presence of temperature fluctuations.

This additional development and refinement of the diagnostic technique can and should occur in the context of a particular application. Working with WRDC, we have identified a two-phase reacting flow experiment where the

techniques demonstrated in the course of this program can benefit the ongoing research effort. Future work should concentrate on additional quantification and validation studies in a flowfield of similar species composition and temperature. This diagnostic development should occur in parallel with application to the actual experimental apparatus, thereby expediting the transfer of the techniques to genuine combustion research programs.

## 6. REFERENCES

1. R.K. Hanson, "Combustion diagnostics: planar imaging techniques," 21st Symposium (Int.) on Combustion (Pittsburgh: The Combustion Institute), p. 1677, 1986.
2. R.K. Hanson, "Planar laser-induced fluorescence imaging," J. Quant. Spectrosc. Radiat. Transfer 40(3), p. 343, 1988.
3. M.G. Allen and R.K. Hanson, "Digital imaging of species concentration fields in spray flames," 21st Symposium (Int.) on Combustion, (The Combustion Institute, Pittsburgh), p. 1755, 1986.
4. G. Kychakoff, R.D. Howe, R.K. Hanson, and J.C. McDaniel, "Quantitative visualization of combustion species in a plane," App. Opt. 21, p. 3225, 1982.
5. I.L. Chidsey and D.R. Crosley, "Calculated rotational transition probabilities for the A-X system of OH," J. Quant. Spectrosc. Radiat. Transfer 23, p. 187, 1980.
6. G.P. Smith and D.R. Crosley, "Quantitative laser-induced fluorescence in OH: transition probabilities and the influence of energy transfer," 18th Symposium (Int.) on Combustion (Pittsburgh: The Combustion Institute), p. 1511, 1981.
7. D.R. Crosley and G.P. Smith, "Rotational energy transfer and LIF temperature measurements," Combustion and Flame 44, p. 27, 1982.
8. G.P. Smith and D.R. Crosley, "Vibrational energy transfer in  $A^2\Sigma^+$  OH in flames," App. Opt. 22(10), p. 1428, 1983.
9. R.A. Copeland, M.L. Wise, and D.R. Crosley, "Vibrational energy transfer and quenching of OH ( $A^2\Sigma^+$ ,  $v' = 1$ )," J. Phys. Chem. 92, p. 5710, 1988.
10. N.L. Garland and D.R. Crosley, "On the collisional quenching of electronically excited OH, NH, and CH in flames," 21st Symposium (Int.) on Combustion (Pittsburgh: The Combustion Institute), p. 1693, 1986.
11. J.B. Jefferies, K. Kohse-Hoinghaus, G.P. Smith, R.A. Copeland, and D.R. Crosley, "Rotational-level dependent quenching of OH ( $A^2\Sigma^+$ ) at flame temperatures," Chem. Phys. Lttrs. 152(2,3), p. 160, 1988.
12. R.S. Barlow, R.W. Dibble, R.P. Lucht "Simultaneous measurement of Raman scattering and laser-induced OH fluorescence in nonpremixed turbulent jet flames," Opt. Lttrs. 14(5), p. 263, 1989.
13. L.G. Piper and L.M. Cowles, "Transition moment variation for NO ( $A^2\Sigma - X^2\Pi$ )" J. Chem. Phys. 85(5), p. 2421, 1986.



14. I.S. McDermid and J.B. Laudenslager, "Radiative lifetimes and electronic quenching rate constants for single-photon-excited rotational levels of NO ( $A^2\Sigma^+$ ,  $v'=0$ )," J. Quant. Spectrosc. Radiat. Transfer 27(5), p. 483, 1982.
15. L.T. Earls, "Intensities in  $2\Pi - 2\Sigma$  transitions in diatomic molecules," Physical Review, 48, p. 423, 1935.
16. G.H. Diecke and H.M. Crosswhite, "The ultraviolet bands of OH," J. Quant. Spectrosc. and Radiat. Transfer 2, p. 97, 1962.
17. R. Engleman, P.E. Rouse, H.M. Peek, V.D. Baiamonte, "Beta and gamma band systems of nitric oxide," Los Alamos Scientific Laboratory Report, LA-4364, July 1970.
18. W.M. Jackson, J.B. Halpern, and C.S. Lin, "Multiphoton ultraviolet photochemistry," Chem. Phys. Letters 55, p. 254, 1978.
19. J.R. McDonald, A.P. Baronavski, and V.M. Donnelly, "Multiphoton-vacuum-ultraviolet laser photodissociation of acetylene: emission from electronically fragments," Chemical Physics 33, p. 161, 1978.
20. B.B. Craig, W.L. Faust, and L.S. Goldberg, "UV short-pulse fragmentation of isotopically labeled acetylene; studies of emission with subnanosecond resolution," J. Chem. Phys. 76, p. 5014, 1982.
21. A.M. Kanury, Introduction to Combustion Phenomena (New York: Gordon and Breach Scientific Publishers), 1977, p. 130.
22. A. Ciajolo, R. Barbella, M. Mattiello, and A.D'Alessio, "Axial and radial measurements of soot and PAH in a light oil flame," 19th Symposium (Int.) on Combustion (Pittsburgh: The Combustion Institute), p. 1369, 1982.
23. R.F. Weber and A. Garscadden, "Errors due to averaging spectral-line intensities in the presence of electron-temperature variations," JOSA 61(10), p. 1330, 1971.
24. M.G. Mungal and P.E. Dimotakis, "Mixing and combustion with low heat release in a turbulent shear layer," J. Fluid Mech. 148, p. 349, 1984.
25. P.H. Paul, M.P. Lee, and R.K. Hanson, "Molecular velocity imaging of supersonic flows using pulsed planar laser-induced fluorescence of NO," Opt. Lett. 14(9), p. 417, 1989.
26. I. Glassman, Combustion (New York: Academic Press) 1977, p. 75.
27. N. Peters, "Laminar Flamelet Concepts in Turbulent Combustion," 21st Symposium (Int.) on Combustion (Pittsburgh: The Combustion Institute), p. 1231, 1986.